A&A 596, A101 (2016)
DOI: 10.1051/0004-6361/201527743
© ESO 2016

Astronomy & Astrophysics

Planck intermediate results

XL. The Sunyaev-Zeldovich signal from the Virgo cluster

Planck Collaboration: P. A. R. Ade[86], N. Aghanim[59], M. Arnaud[73], M. Ashdown[69,5], J. Aumont[59], C. Baccigalupi[85], A. J. Banday[95,10], R. B. Barreiro[64], N. Bartolo[28,65], E. Battaner[97,98], K. Benabed[60,93], A. Benoit-Lévy[22,60,93], J.-P. Bernard[95,10], M. Bersanelli[31,49], P. Bielewicz[81,10,85], A. Bonaldi[67], L. Bonavera[64], J. R. Bond[9], J. Borrill[13,89], F. R. Bouchet[60,87], C. Burigana[48,29,50], R. C. Butler[48], E. Calabrese[91], J.-F. Cardoso[74,1,60], A. Catalano[75,72], A. Chamballu[73,14,59], H. C. Chiang[25,6], P. R. Christensen[82,35], E. Churazov[79,88], D. L. Clements[56], L. P. L. Colombo[21,66], C. Combet[75], B. Comis[75], F. Couchot[71], A. Coulais[72], B. P. Crill[66,11], A. Curto[64,5,69], F. Cuttaia[48], L. Danese[85], R. D. Davies[67], R. J. Davis[67], P. de Bernardis[30], A. de Rosa[48], G. de Zotti[45,85], J. Delabrouille[1], C. Dickinson[67], J. M. Diego[64,*], K. Dolag[96,79], H. Dole[59,58], S. Donzelli[49], O. Doré[66,11], M. Douspis[59], A. Ducout[60,56], X. Dupac[38], G. Efstathiou[61], F. Elsner[22,60,93], T. A. Enßlin[79], H. K. Eriksen[62], F. Finelli[48,50], O. Forni[95,10], M. Frailis[47], A. A. Fraisse[25], E. Franceschi[48], S. Galeotta[47], S. Galli[68], K. Ganga[1], M. Giard[95,10], Y. Giraud-Héraud[1], E. Gjerløw[62], J. González-Nuevo[18,64], K. M. Górski[66,99], A. Gregorio[32,47,53], A. Gruppuso[48], J. E. Gudmundsson[92,25], F. K. Hansen[62], D. L. Harrison[61,69], G. Helou[11], C. Hernández-Monteagudo[12,79], D. Herranz[64], S. R. Hildebrandt[66,11], E. Hivon[60,93], M. Hobson[5], A. Hornstrup[15], W. Hovest[79], K. M. Huffenberger[23], G. Hurier[59], A. H. Jaffe[56], T. R. Jaffe[95,10], W. C. Jones[25], E. Keihänen[24], R. Keskitalo[13], T. S. Kisner[77], R. Kneissl[37,7], J. Knoche[79], M. Kunz[16,59,2], H. Kurki-Suonio[24,43], G. Lagache[4,59], J.-M. Lamarre[72], A. Lasenby[5,69], M. Lattanzi[29], C. R. Lawrence[66], R. Leonardi[8], F. Levrier[72], M. Liguori[28,65], P. B. Lilje[62], M. Linden-Vørnle[15], M. López-Caniego[38,64], P. M. Lubin[26], J. F. Macías-Pérez[75], B. Maffei[67], G. Maggio[47], D. Maino[31,49], N. Mandolesi[48,29], A. Mangilli[59,71], A. Marcos-Caballero[64], M. Maris[47], P. G. Martin[9], E. Martínez-González[64], S. Masi[30], S. Matarrese[28,65,41], P. Mazzotta[33], P. R. Meinhold[26], A. Melchiorri[30,51], A. Mennella[31,49], M. Migliaccio[61,69], S. Mitra[55,66], M.-A. Miville-Deschênes[59,9], A. Moneti[60], L. Montier[95,10], G. Morgante[48], D. Mortlock[56], D. Munshi[86], J. A. Murphy[80], P. Naselsky[83,36], F. Nati[25], P. Natoli[29,3,48], F. Noviello[67], D. Novikov[78], I. Novikov[82,78], N. Oppermann[9], C. A. Oxborrow[15], L. Pagano[30,51], F. Pajot[59], D. Paoletti[48,50], F. Pasian[47], T. J. Pearson[11,57], O. Perdereau[71], L. Perotto[75], V. Pettorino[42], F. Piacentini[30], M. Piat[1], E. Pierpaoli[21], S. Plaszczynski[71], E. Pointecouteau[95,10], G. Polenta[3,46], N. Ponthieu[59,54], G. W. Pratt[73], S. Prunet[60,93], J.-L. Puget[59], J. P. Rachen[19,79], M. Reinecke[79], M. Remazeilles[67,59,1], C. Renault[75], A. Renzi[34,52], I. Ristorcelli[95,10], G. Rocha[66,11], C. Rosset[1], M. Rossetti[31,49], G. Roudier[1,72,66], J. A. Rubiño-Martín[63,17], B. Rusholme[57], M. Sandri[48], D. Santos[75], M. Savelainen[24,43], G. Savini[84], B. M. Schaefer[94], D. Scott[20], J. D. Soler[59], V. Stolyarov[5,90,70], R. Stompor[1], R. Sudiwala[86], R. Sunyaev[79,88], D. Sutton[61,69], A.-S. Suur-Uski[24,43], J.-F. Sygnet[60], J. A. Tauber[39], L. Terenzi[40,48], L. Toffolatti[18,64,48], M. Tomasi[31,49], M. Tristram[71], M. Tucci[16], G. Umana[44], L. Valenziano[48], J. Valiviita[24,43], B. Van Tent[76], P. Vielva[64], F. Villa[48], L. A. Wade[66], B. D. Wandelt[60,93,27], I. K. Wehus[66], J. Weller[96], D. Yvon[14], A. Zacchei[47], and A. Zonca[26]

(Affiliations can be found after the references)

Received 13 November 2015 / Accepted 27 September 2016

ABSTRACT

The Virgo cluster is the largest Sunyaev-Zeldovich (SZ) source in the sky, both in terms of angular size and total integrated flux. *Planck*'s wide angular scale and frequency coverage, together with its high sensitivity, enable a detailed study of this big object through the SZ effect. Virgo is well resolved by *Planck*, showing an elongated structure that correlates well with the morphology observed from X-rays, but extends beyond the observed X-ray signal. We find good agreement between the SZ signal (or Compton parameter, y_c) observed by *Planck* and the expected signal inferred from X-ray observations and simple analytical models. Owing to its proximity to us, the gas beyond the virial radius in Virgo can be studied with unprecedented sensitivity by integrating the SZ signal over tens of square degrees. We study the signal in the outskirts of Virgo and compare it with analytical models and a constrained simulation of the environment of Virgo. *Planck* data suggest that significant amounts of low-density plasma surround Virgo, out to twice the virial radius. We find the SZ signal in the outskirts of Virgo to be consistent with a simple model that extrapolates the inferred pressure at lower radii, while assuming that the temperature stays in the keV range beyond the virial radius. The observed signal is also consistent with simulations and points to a shallow pressure profile in the outskirts of the cluster. This reservoir of gas at large radii can be linked with the hottest phase of the elusive warm/hot intergalactic medium. Taking the lack of symmetry of Virgo into account, we find that a prolate model is favoured by the combination of SZ and X-ray data, in agreement with predictions. Finally, based on the combination of the same SZ and X-ray data, we constrain the total amount of gas in Virgo. Under the hypothesis that the abundance of baryons in Virgo is representative of the cosmic average, we also infer a distance for Virgo of approximately 18 Mpc, in good agreement with previous estimates.

Key words. ISM: general – galaxies: clusters: individual: Virgo – galaxies: clusters: intracluster medium – cosmic background radiation – large-scale structure of Universe

1. Introduction

The Virgo cluster is the closest cluster to our Galaxy (smaller groups like Leo are closer but are significantly less massive). Virgo is a moderate cluster in terms of its mass, $M \approx (4\text{–}8) \times 10^{14}\ M_\odot$ (de Vaucouleurs 1960; Hoffman et al. 1980; Böhringer et al. 1994; Karachentsev & Nasonova 2010; Karachentsev et al. 2014), but it is the biggest cluster in terms of angular size (tens of square degrees). The combination of moderate mass and large angular size makes this cluster the most prominent single source

* Corresponding author: J. M. Diego,
e-mail: jdiego@ifca.unican.es

Article published by EDP Sciences, to be cited as http://dx.doi.org/10.1051/0004-6361/201527743

for the Sunyaev-Zeldovich (SZ) effect in the sky in terms of integrated flux (Taylor et al. 2003). The Coma cluster, on the other hand, is the most prominent cluster in terms of signal-to-noise (Planck Collaboration Int. X 2013) but subtends a significantly smaller solid angle than Virgo.

Despite its significant total flux, the strength of the SZ signal (or more specifically the surface brightness) is expected to be low for this moderate mass cluster, as shown by Diego & Ascasibar (2008), making it a challenging object to study.

Owing to its proximity to us (distance between 15 Mpc and 21 Mpc; Sandage & Tammann 1976; Freedman et al. 1994; Pierce et al. 1994; Federspiel et al. 1998; Graham et al. 1999; Tammann et al. 2000; Jerjen et al. 2004; Mei et al. 2007), Virgo presents a unique opportunity to use *Planck*[1] to study the SZ effect in the outskirts of clusters with *Planck*.

The angular size of the virial radius, $R_{\rm vir}$, of Virgo is 4° (for consistency we adopt the same virial radius, $R_{\rm vir}$, as Urban et al. 2011) corresponding to 1 Mpc (for a distance of $D = 15$ Mpc). The area enclosed between $R_{\rm vir}$ and 1.25 $R_{\rm vir}$ is an impressive 30 deg^2. No other cluster offers such a large area, enabling us to average the SZ signal and increase the sensitivity to an unprecedented level. Hence, the Virgo cluster offers a unique opportunity to study the elusive warm/hot intergalactic medium (or WHIM), which is believed to exist around clusters and has, so far, evaded a clear detection. WHIM gas is expected to have temperatures of 10^5–10^7 K and densities of 10–30 times the mean density of the Universe (Davé et al. 2001). The strength of the SZ signal around Virgo owing to the WHIM is expected to be of the order of a microkelvin at the relevant *Planck* frequencies as shown by Diego & Ascasibar (2008). This level of sensitivity in the outskirts of clusters can be reached with *Planck* only after averaging big areas of the sky. This, in turn, is possible only in the Virgo cluster, which subtends such a sizable solid angle (tens of deg^2) while other clusters subtend areas of the order of 1 deg^2 at most (with Coma a little above this number). The evidence of ram pressure acting in the outskirts of Virgo (Kenney et al. 2004) also supports the hypothesis that vast amounts of gas are still present at these distances from the centre and hence possibly detectable by *Planck*.

Combining SZ and X-ray observations. The full-sky coverage and wide frequency range of *Planck* makes it an ideal instrument to study the SZ effect in big objects like Virgo (Planck Collaboration VIII 2011; Planck Collaboration IX 2011; Planck Collaboration X 2011). *Planck* performs better than ground-based experiments when studying diffuse SZ signals that extend over relatively large angular scales. Ground-based observations at large angular scales are affected by atmospheric fluctuations, which need to be removed. Yet the removal of this distorts the modes that include the signal on large angular scales. *Planck* data do not suffer from these limitations, and hence diffuse, low-surface brightness objects can be resolved and detected by *Planck*, providing their solid angle is big enough. The main limitations of *Planck* data are Galactic foregrounds and the cosmic microwave background (CMB) signal; however, the frequency coverage and sensitivity of *Planck* enable the detailed foreground and CMB removal that is necessary to study this cluster.

The proximity of Virgo to us also enables detailed studies in other bands. Of particular interest are the results derived from X-rays, since they trace the same plasma that is responsible for the SZ effect. Virgo is also the brightest cluster in terms of integrated X-ray flux. It has been studied in detail by different X-ray observatories (ROSAT, *XMM-Newton*, *Chandra*, and *Suzaku*), although only ROSAT, with its full-sky coverage, provides a complete picture of Virgo and its surroundings. On the other hand, the superior resolution of *XMM-Newton* and *Chandra* has allowed more detailed studies of the inner structure of Virgo or to estimate the metallicity up to the virial radius with *Suzaku* (Simionescu et al. 2015). In particular, Ghizzardi et al. (2004, G04 hereafter) present an analysis of the central 100 kpc region around M 87 (with *Chandra* and *XMM-Newton* X-ray data). Using *XMM-Newton* data (Urban et al. 2011, U11 hereafter) study the X-ray emission in Virgo out to the virial radius ($R_{\rm vir} \approx 1$ Mpc), but only through a narrow sector of the Virgo cluster.

When combined with X-ray data, the SZ signal from *Planck* has the potential to discriminate between different models of the pressure that are indistinguishable with X-ray data alone. This fact is exploited in this paper, as one of its main objectives, to infer properties of the distribution of the plasma in this cluster. Also, the possibility to resolve Virgo with *Planck* and hence to study different regions independently allows for a more detailed study of these regions. Due to the different dependencies of the SZ effect and X-ray emission on the electron density, resolved images also allow us to test possible deviations from a smooth distribution of the plasma.

Clumpiness is expected to result in an overestimation of the observed gas density based on X-ray data in the outskirts of clusters (Nagai & Lau 2011). Although the increased angular resolution provided by the recent X-ray observatories, in particular *Chandra*, has constrained the amount of clumpiness in the central region of the cluster (Werner et al. 2016), and *XMM-Newton* at longer distances, see Urban et al. (2011), it is interesting to study possible differences between the predicted SZ effect based on X-ray-derived models and the SZ signal observed by *Planck*. The relative proximity of Virgo means that at the resolution of *Planck* any features bigger than 26 kpc (or 4.5 arcmin) can potentially be resolved. This is an unprecedented resolution for galaxy cluster studies using *Planck* data. As opposed to other typical clusters, the geometry of Virgo reveals a complex structure with different clumps being separated by up to several megaparsecs (Jerjen et al. 2004).

The Virgo Cluster. At the centre of Virgo is M 87, one of the most powerful known AGN, flanked by two very luminous radio jets. The radio emission marks the regions where significant amounts of energy are being injected into the cluster medium. In X-rays, cold fronts and shock waves have been identified that are also linked to the extraordinary activity of the supermassive black hole at the centre of M 87. Perhaps the clearest evidence of the extreme activity surrounding M 87 is the presence of radio lobes with a geometry that suggests sub-sonic injection of colder gas into the intracluster medium (Churazov et al. 2001; Forman et al. 2007). The activity of the AGN has an impact on the X-ray emissivity of the surrounding gas at supergalactic scales (Werner et al. 2010).

As a theoretical counterpart, we use the Virgo cluster from a constrained simulation of the local Universe. We adopt the

[1] *Planck* (http://www.esa.int/Planck) is a project of the European Space Agency (ESA) with instruments provided by two scientific consortia funded by ESA member states and led by Principal Investigators from France and Italy, telescope reflectors provided through a collaboration between ESA and a scientific consortium led and funded by Denmark, and additional contributions from NASA (USA).

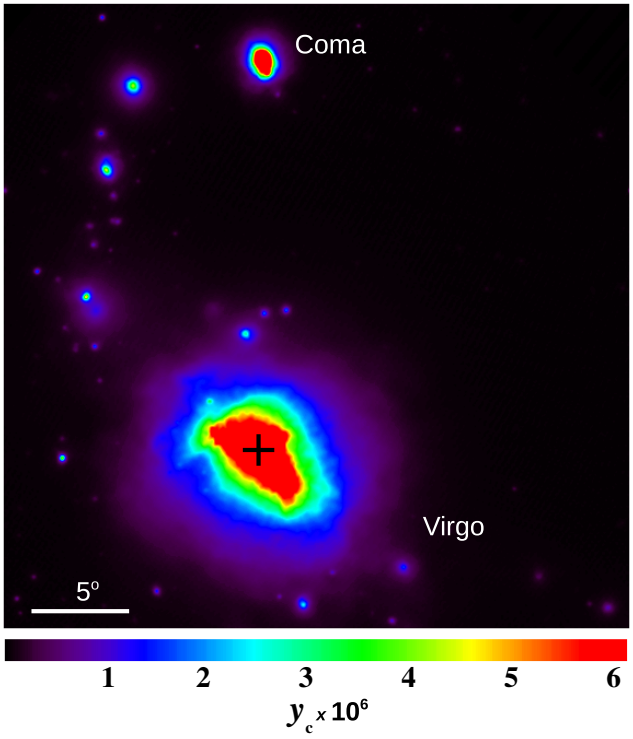

Fig. 1. Simulated Virgo cluster (indicated by a black cross) from a constrained simulation in units of 10^{-6} times the Compton parameter (Dolag et al. 2005). To increase the contrast, the Compton parameter beyond 6×10^{-6} has been saturated. The brightest cluster in the top is Coma. In this and other figures (unless otherwise noted) the coordinates are Galactic, the projection is orthographic, and the field of view is 31.°94 across or 8.3 (11.9) Mpc assuming Virgo is at a distance of 15 (21.4) Mpc. The North Galactic pole is up and Virgo's centre (M 87) is 4° south of the centre of the images.

initial conditions from Mathis et al. (2002), who perform N-body numerical simulations and demonstrated that the evolved state of these initial conditions provides a good match to the large-scale structure observed in the local Universe. Here, many of the most prominent nearby clusters (among them Virgo and Coma) can be identified directly with halos in the simulations, with a good agreement for sky position and virial mass. Dolag et al. (2005) repeated these simulations including also the baryonic component, demonstrating that the simulated SZ signal reproduces the expected SZ signal. In this work we use a new simulation that includes a wealth of physical processes known to be important to reproduce realistic galaxy clusters (Hirschmann et al. 2014), most importantly the feedback from star formation and from super-massive black holes. We use an implementation that also matches various observed properties of AGN, as described in the work of Hirschmann et al. (2014), where details of the implemented physical processes can be found.

This physical treatment within the simulations results in averaged pressure profiles, which match well the observed ones from *Planck*, as demonstrated in Planck Collaboration Int. V (2013). However, one has to keep in mind that the uncertainties in the construction of the initial conditions are still substantial, so that the details of the Virgo cluster formed in the simulations will be different from the real, observed one. Especially given that the current state of the AGN in the centre of the simulated Virgo cluster is not constrained at all, we therefore expect significant differences particularly in the central part. Figure 1 shows the region of the sky that contains the simulated Virgo and Coma clusters in units of the Compton parameter, y_c,

$$y_c = \frac{\sigma_T \, k_B}{m_e \, c^2} \int n_e \, T \, \mathrm{d}l \qquad (1)$$

where the integral is along the line of sight and σ_T, k_B, m_e, n_e, and T are the Thomson cross section, Boltzmann constant, mass of the electron, electron density, and electron temperature, respectively.

The positions of Virgo and other simulated clusters in the field of view in Fig. 1 are approximately the same as the actual ones in the real world, as seen in previous studies (Mathis et al. 2002; Dolag et al. 2005). The image shows the Compton parameter, y_c, and has been saturated above $y_c = 6 \times 10^{-6}$ for contrast purposes. When compared with Coma (the highest signal-to-noise (S/N) SZ source in the sky), it is evident that despite its low surface brightness, Virgo is expected to be the brightest source in terms of integrated signal. Also from the same figure, it is evident that the outskirts of the Virgo cluster cover a significant area of many square degrees, where the elusive WHIM could be detected after integrating over this big area. Some evidence of its existence already exists from observations (e.g., Yoon et al. 2012).

The resolution of *Planck* does not allow us to study the pressure profile of clusters in detail, since most of them appear unresolved or barely resolved. A few exceptions, like the Coma cluster, have allowed a study of the pressure profile of clusters in more detail (Planck Collaboration Int. X 2013). However, Virgo is a significantly less massive cluster (for which SZ effect observations are rare) and offers a unique opportunity to study the pressure profile in a moderate-mass system, for which the constraints are poor. The pressure profile has also been studied with *Planck* in a sample of 62 nearby massive clusters detected at high significance with *Planck* and with good ancillary X-ray data (Planck Collaboration Int. V 2013).

Virgo allows us to extend the study of the pressure profile to the poorly explored regime of low to moderate-mass clusters and also to extend the distances at which the pressure can be observed. This constitutes a primary objective of the current paper.

Given its relative proximity to us, a distance estimate based on the redshift of the galaxies within Virgo can be inaccurate due to the peculiar velocities of those galaxies and/or our own movement towards Virgo. On the other hand, the distance to Virgo is big enough that distance measurements based on Cepheids or planetary nebulae are also difficult to make. As a consequence, the absolute distance of the Virgo cluster is still a matter of debate, with measurements from various techniques (Cepheids, globular clusters, planetary nebulae, surface brightness fluctuations, and supernovae) resulting in a range of distances for Virgo ranging from 15 Mpc to 21 Mpc (Sandage & Tammann 1976; Freedman et al. 1994; Pierce et al. 1994; Federspiel et al. 1998; Graham et al. 1999; Tammann et al. 2000; Jerjen et al. 2004; Mei et al. 2007). Part of the discrepancy may be due to the distribution of spiral galaxies in the field of view, which concentrate in an elongated region extending from 13 to 30 Mpc, closely aligned with the line of sight. This affects the distance moduli estimated based on Tully-Fisher analyses (Fukugita et al. 1993). Following G04, and in order to keep consistency with that work, we adopt a default distance of 21 Mpc for the computation of the X-ray count rate and the conversion from physical to angular scales. The implications of adopting a different distance are discussed in Sect. 7.3, where we also derive an independent distance estimate based on the combined SZ and X-ray observations.

The paper is organized as follows. Section 2 gives a brief description of the *Planck* data used for this study. In Sect. 3 we

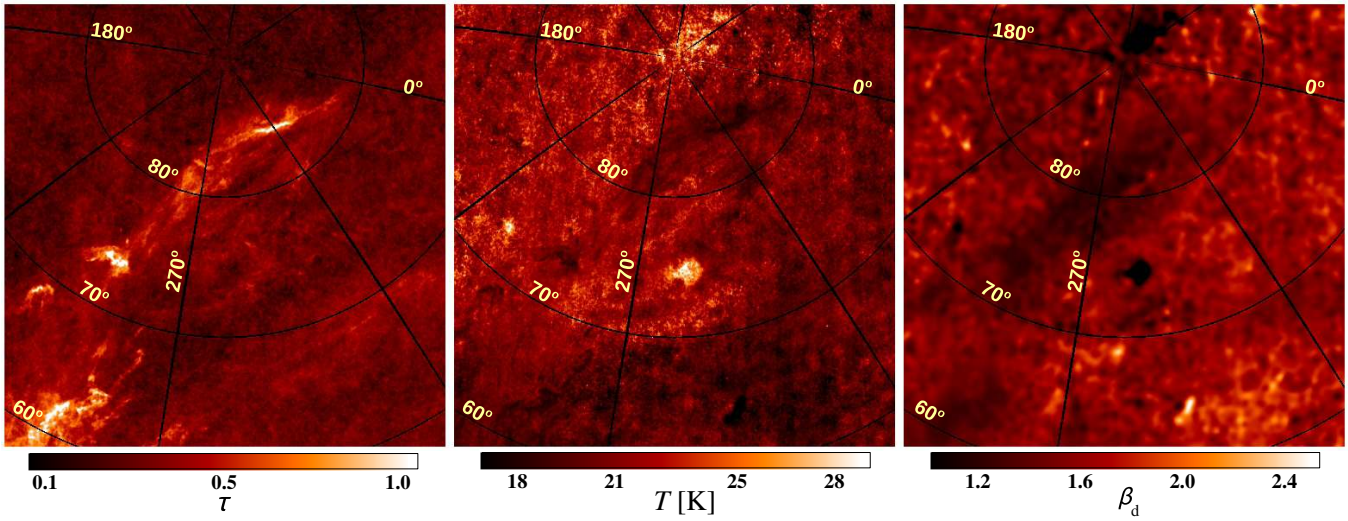

Fig. 2. *Left to right*: optical depth τ, dust temperature T (in kelvin), and spectral index β_d of the dust component in the Virgo region. Some clusters in this field of view (Coma to the north, Leo to the east, and Virgo near the centre) can be clearly spotted as artefacts in the T and β_d maps. The coordinates are Galactic and the field of view resembles that of Fig. 1 (31°.9) and other figures in this paper.

describe the data analysis and potential sources of systematics that could affect the extraction of the SZ signal from *Planck* data. Section 4 describes the X-ray ROSAT observations of Virgo. In Sect. 5 we model the SZ effect and X-ray emission from the cluster and discuss the models derived from *XMM-Newton* and *Chandra*. Section 6 presents results on standard radial profiles of the SZ and X-ray data and a comparison with different models. In Sect. 7 we focus our attention on the signal beyond the virial radius and constrain the distance to Virgo from the combination of SZ and X-ray data. Finally, we present the conclusions in Sect. 8.

2. *Planck* data

Planck's sensitivity, angular resolution, and frequency coverage make it a powerful instrument for Galactic and extragalactic astrophysics as well as cosmology. An overview of the latest results from *Planck* can be found in Planck Collaboration I (2016). This paper is based on *Planck*'s full survey mission, where the whole sky has been covered over 5 times by the high frequency instrument (HFI) and 8 times by the low frequency instrument (LFI). We refer to Planck Collaboration II (2016), Planck Collaboration III (2016), Planck Collaboration IV (2016), Planck Collaboration V (2016), Planck Collaboration VI (2016), Planck Collaboration VII (2016) and Planck Collaboration VIII (2016) for technical information about the calibration, processing of the data, mapmaking, instrument response, and beams of the two instruments, LFI and HFI. For this particular work, we rely on the *Planck* bands at 70, 100, 143, 217, and 353 GHz. However, the bands at 545 and 857 GHz are also used to test for Galactic residuals.

From the full-sky *Planck* maps, we extract square patches of 31°.9 × 31°.9 containing the Virgo cluster. The centre of the field of view is chosen such that other prominent clusters (like nearby Coma) are also included in the field of view for comparison. Other smaller, but still prominent, clusters like the Leo cluster also fall in our field of view. We extract patches of *Planck*'s LFI and HFI data, as well as ancillary data (e.g., NVSS, IRAS, and ROSAT). The ancillary data are used to check for possible systematic effects (contamination from radio or infrared point sources, Galactic contamination or Galactic dust variability) but also to use these data in combination with *Planck* (in particular ROSAT). Patches from the "half-ring" differences and each individual survey (eight for LFI and five for HFI) are also extracted to study possible systematic effects and to understand the properties of the noise maps.

3. Extracting the SZ effect in Virgo from *Planck* data

To isolate the SZ effect from Virgo, the dominant signals from the CMB and the Galaxy need to be removed. As shown in Fig. 2, the Galactic emission around the Virgo cluster exhibits a complex pattern, with significant variations in the optical depth τ, dust temperature T_d, and spectral index (of a modified blackbody model) β_d. In the optically thin limit, the specific intensity I_ν from a population of grains is well approximated by a modified blackbody,

$$I_\nu \propto \tau\, \nu^{\beta_d}\, B(\nu, T_d), \tag{2}$$

where $B(\nu, T_d)$ is the Planck blackbody function. From Fig. 2 the dust temperature ranges from 18 to 28 K, while the emissivity index, β_d, runs from 1 to 2.4. The temperature and spectral index are derived from the combination of the 353 GHz, 545 GHz, 857 GHz *Planck* bands and the 100 μm IRAS band, which are fit to the form of Eq. (2) after subtraction of an average (constant) estimate of the background (CIB) levels and the CMB (see Planck Collaboration XI 2014). Figure 2 summarizes some of the main challenges in our analysis arising from the complexity of the Galactic contamination around Virgo. There is a distinctive filamentary feature in the north-west (extending from $\ell \approx 250°$, $b \approx 60°$ to $\ell \approx 330°$, $b \approx 85°$) with a lower temperature and higher spectral index, crossing relatively close to the northern part of Virgo. A ring of diffuse Galactic dust also surrounds the centre of the Virgo region. In addition, although not evident in these maps, the zodiacal light extends horizontally in the bottom part of our field of view, although most of its contribution can be removed together with the Galaxy, since its spectral behaviour is very similar to Galactic emission. The 217 GHz band, critical for the removal of the CMB, is still significantly contaminated by Galactic dust (seen clearly, for instance, in the difference between the 217-GHz and 143-GHz maps of

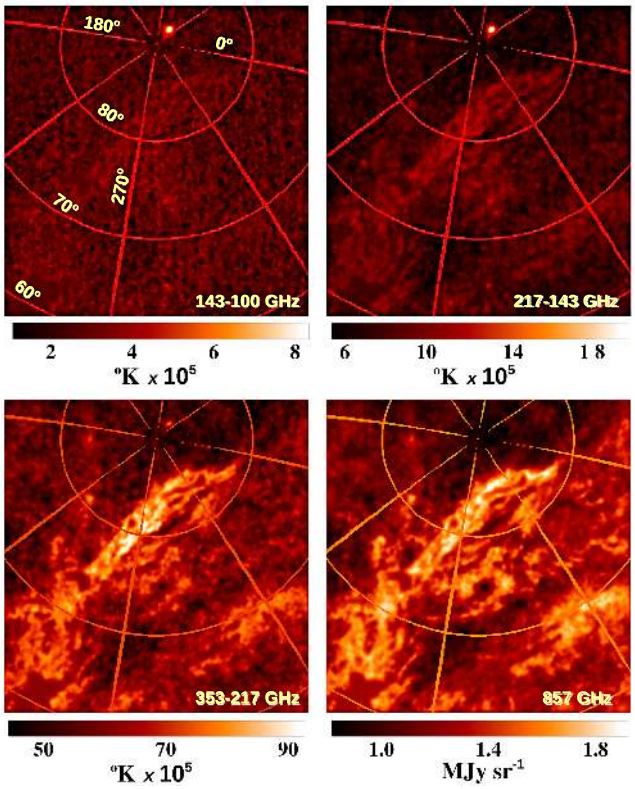

Fig. 3. Differences (in kelvin) between the individual *Planck* bands. The *lower right panel* shows the original data at 857 GHz (in MJy sr^{-1}). All maps have been masked and degraded to the same resolution before calculating the differences. In all differences the SZ effect should appear as a positive signal. The Coma cluster is clearly visible in the top of the images of the low-frequency differences.

Fig. 3). In standard SZ maps produced via an internal linear combination (ILC) it is generally assumed that there is no spatial variability in the dust spectral index or the temperature, so some residual Galactic contamination is expected to remain in the SZ maps. Instead of producing an ILC SZ map, the temperature and spectral index information could, in principle, be used to overcome this problem by taking their spatial variability into account. However, the SZ signal itself contaminates the estimates of the dust temperature and spectral index at the positions of clusters, resulting in high temperature and low spectral index, as shown in Fig. 2 at the positions of Coma and Virgo. A third cluster, Leo, is also clearly seen to the East in the temperature and spectral index maps.

3.1. Internal Linear Combination for Virgo

The Virgo cluster is clearly seen in the latest *Planck* maps of the thermal SZ effect (Planck Collaboration XXII 2016). Although these maps provide a high-quality all-sky vision of the SZ effect at all scales, certain regions in the sky are still contaminated by Galactic residuals. These could be reduced by performing a specific component separation in that region. Due to the Galactic contamination, we use a specific and tailored ILC method to produce the SZ map for Virgo. First, we use only the *Planck* maps that contain the least amount of Galactic contamination. In particular, in our analysis we do not use the maps at 545 and 857 GHz, frequently used in other ILC methods in *Planck* e.g. in `MILCA` (Hurier et al. 2013) and `NILC` (Delabrouille et al. 2009; Remazeilles et al. 2011), as tracers of the Galactic dust. Due to variations in the dust spectral index and temperature, these maps introduce spurious residuals when combined with (or extrapolated to) low frequencies. Second, we avoid filtering of the large scales in the maps. The filtering is normally used in standard ILC maps like `MILCA` and `NILC` to reduce the negative impact of large-scale Galactic residuals.

Since Virgo is a very extended source spanning many degrees, this filtering process could remove some of the large-scale features of Virgo. Instead, we produce individual SZ effect maps (at 70, 100, and 143 GHz) by removing an estimate of the CMB, an estimate of the Galactic dust, and masking residual point sources. The estimate of the CMB is defined as a Galaxy-clean version of the 217 GHz map, as described below. The estimate of the Galactic dust is obtained from simple differences of frequency bands (also described in more detail below). No model or template is assumed for either the Galaxy or the CMB and the SZ effect map is the result of a pure combination of *Planck* maps (ILC) without any filtering in Fourier space (other than the degradation of the different maps to a common resolution). To derive the SZ effect map we use the *Planck* data at 70, 100, 143, 217, and 353 GHz.

The band at 217 GHz is particularly interesting because the thermal SZ is nearly zero in this band and it is dominated by CMB and Galactic foregrounds, our main sources of contamination for the SZ signal. All maps are degraded to a common resolution of 15′ (FWHM) so the final SZ effect map is obtained also with a resolution of 15′. This resolution is typically poorer than that used in previous analyses of the SZ effect in *Planck* data, where the typical resolution of the SZ effect map is between 5′ and 10′. In the particular case of Virgo, given its big angular size, degrading the maps to 15′ allows for the inclusion of the 70 GHz band, which is relevant for SZ effect studies. Our final SZ effect map is obtained as a weighted combination of the individual SZ effect maps obtained at 70, 100, and 143 GHz (after using the 217 GHz and 353 GHz data to clean the maps of CMB and Galactic emission).

More precisely, the cleaning process (i.e., the removal of the CMB and the Galaxy) is divided into three steps.

1. A template for the Galaxy is obtained from the *Planck* frequency maps (see below for details) and this template is used to clean the 217 GHz band from Galactic residual and produce a *clean* map at 217 GHz.
2. The clean 217 GHz band is taken as an estimate of the CMB that is subtracted from the other maps (70, 100, and 143 GHz), producing individual estimates of the SZ effect that still contain Galactic residuals (plus instrumental noise and point source residuals) at the different frequencies. These Galactic residuals are reduced by using another alternative dust template ($D_{\rm T}$, see below), resulting in the three final SZ maps at 70, 100, and 143 GHz.
3. The three SZ maps are combined to produce a single SZ map in units of the Compton parameter.

The final SZ map is dominated by SZ signal, but also contains instrumental noise, stripe structures due to baseline removal, and Galactic and extragalactic residuals. In summary, the SZ effect map at a given frequency ν (with ν = 70, 100, or 143 GHz), is given by

$$\mathrm{SZ}_\nu = M_\nu - M^{\rm c}_{217} - C_\nu\, D_{\rm T}, \qquad (3)$$

where M_ν is the *Planck* map at frequency ν, $M^{\rm c}_{217}$ is the dust-cleaned 217 GHz *Planck* map containing CMB, kinetic SZ effect, thermal SZ effect (see discussion below), and Galactic

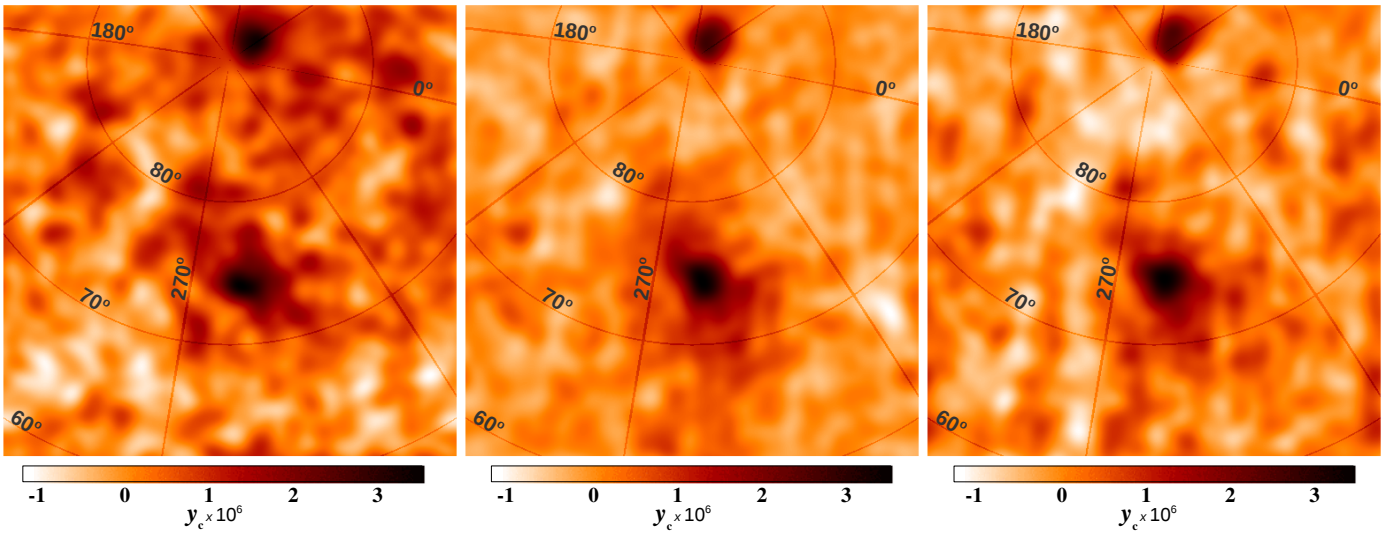

Fig. 4. *Left to right*: individual SZ maps at 70, 100, and 143 GHz in units of 10^6 times the Compton parameter. The field of view is 31.°9 and the coordinates are Galactic. Virgo is the extended source below the centre. The Coma cluster is also clearly visible in the top of the map. The maps have been smoothed to a resolution of 1.°5 to highlight the faintest structures.

residuals, which are reduced by subtracting a template for the Galaxy, D_T. The coefficient C_ν is found by minimizing the residuals in the region of the SZ_ν map not containing SZ signal (i.e., known clusters). The dust-cleaned map, M^c_{217}, is defined as $M^c_{217} = M_{217} - A\,(M_{353} - M_{100})$, where the coefficient A is found by minimizing the Galaxy-dominated variance of the difference $M^c_{217} - M_{100}$. We find that a value of $A = 0.142$ produces a map at 217 GHz with a minimal amount of residual Galactic foreground in the Virgo region (in a different region the optimal value for A may differ). We have tested that the value of the coefficient A remains stable when using the CMB from one of the official *Planck* CMB maps (from the *SEVEM* method, Leach et al. 2008; Fernández-Cobos et al. 2012) instead of M_{100}. However, it is important to note that at the positions of the clusters, the *SEVEM* CMB template (and the other official *Planck* CMB templates) are still contaminated by SZ signal. An alternative definition of M^c_{217}, using the M_{143} map instead of M_{100}, gives nearly identical results. Since M^c_{217} involves the difference $M_{353} - M_{100}$ (or alternatively $M_{353} - M_{143}$), this difference contains a significant amount of SZ signal that needs to be accounted for in the final SZ map. We account for the SZ effect contained in this difference in the final SZ effect map when combining the individual SZ effect maps and transforming into Compton parameter units. This correction involves computing the effective response, $F(\nu)$, for each frequency (70, 100 and 143 GHz) and dividing each individual SZ map (at 70, 100 and 143 GHz and given in temperature units) by the corresponding effective response, to produce an SZ map in Compton parameter units. The effective response is defined as

$$F(\nu) = f(\nu) - f(217\ \mathrm{GHz})^c - C_\nu \times (f(353\ \mathrm{GHz}) - f(217\ \mathrm{GHz})^c) \quad (4)$$

where $f(\nu)$ is the frequency dependence of the SZE ($\Delta T(\nu) = y_c f(\nu)$) and C_ν are the same coefficients as in Eq. (3). At 217 GHz, the factor $f(217\ \mathrm{GHz})^c$ is computed as $f(217\ \mathrm{GHz})^c = f(217\ \mathrm{GHz}) - A[f(353\ \mathrm{GHz}) - f(100\ \mathrm{GHz})]$ to account for the SZE residual in the *clean* map at 217 GHz. The coefficient A was described above in the definition of M^c_{217}. Owing to the relatively small temperature of Virgo, we neglect relativistic effects when computing $f(\nu)$.

Finally, the Galaxy template is given by $D_T = M_{353} - M^c_{217}$. As above, this difference also contains a non-negligible amount of SZ effect that is accounted for in the final SZ effect map, as described above. In Fig. 3 we show some of these differences, where the dust contribution can be appreciated even at low frequencies (see, e.g., the 143−100 GHz difference). Although the Galaxy template removes most of the Galactic component, some Galactic residuals still persist and may contaminate the SZ signal. These residuals are discussed below in Sect. 3.3.

The Galaxy template differs from more standard ILC methods that would consider the high-frequency bands at 545 and 857 GHz (or a model based on a combination of bands) as a tracer of the dust at lower frequencies. Our choice is mostly motivated by the variations in the temperature and spectral index of the dust across our field of view and also by the fact that low temperature Galactic regions (which are poorly constrained if they are too faint) may become more important at lower frequencies. Instead of using a Galaxy template defined at high frequencies, we use the Galaxy template defined by the difference between the 353 GHz and 217 GHz bands. This difference is the closest in frequency to the key SZ effect frequencies (70, 100, and 143 GHz). When cleaning the 217 GHz band from dust, we use a different definition for the Galaxy template, taking instead the difference $M_{353} - M_{100}$ (or $M_{353} - M_{143}$). This is done to avoid introducing correlated noise between the 217 GHz band and the Galaxy template. Using the high-frequency bands of *Planck* at 545 and 857 GHz as Galaxy templates has the advantage of yielding a higher S/N and relatively smaller CMB and SZ effect components, but would introduce unwanted Galactic residuals in those Galactic regions with lower temperatures (which are not mapped well by the high frequency bands). Relying on the difference $M_{353} - M_{217}$ (or $M_{353} - M_{100}$) minimizes this problem, since this difference better captures the colder Galactic features present at lower frequencies. Given the large area of Virgo and variations in the dust properties, it is safer to extrapolate a noisier estimate of the Galaxy from 353 GHz to 217 GHz than to extrapolate a higher-S/N version of the Galaxy (but also less accurate

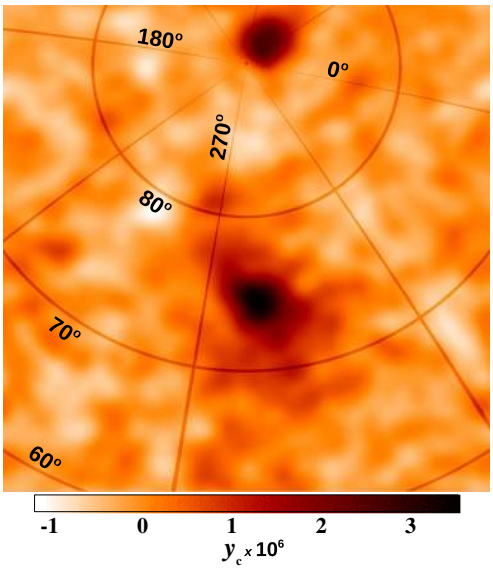

Fig. 5. Virgo SZ map showing its position and extent in Galactic coordinates. The Compton parameter y_c is plotted here. The resolution is 1.°5.

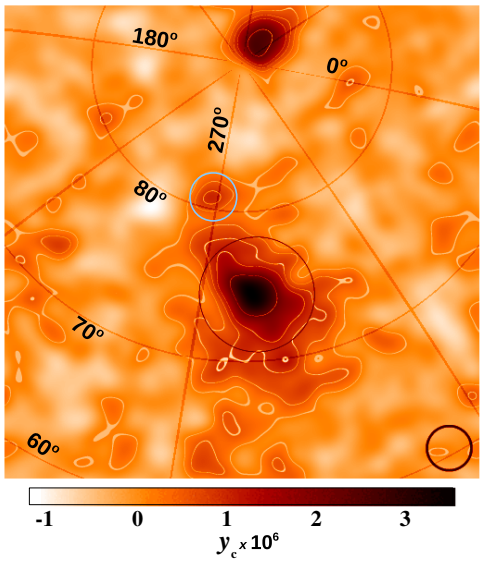

Fig. 6. SZ effect map obtained after combining the individual maps in Fig. 4 and after reducing the impact of stripes (see Appendix A). The colour scale is the same as in Fig. 5. The contours are proportional to 1, 2, 3, 4, and 7 times the dispersion of the background. We only show the contours for the positive (negative in the map) fluctuations of the Compton parameter. Virgo's centre (M 87) is 4° south of the centre of the image and the Coma cluster is clearly seen at the top (i.e., north). Other clusters like the Leo cluster (or group) can also be appreciated near the east edge of the image (in the middle). The big black circle around Virgo marks the area enclosed within the virial radius (3.°9). The small circle at the bottom right has a diameter equal to the FWHM of the Gaussian kernel used to smooth the image (1.°5). The small light-blue circle at $\ell \approx 270°, b \approx 80°$ marks the position of a feature in the SZ map that is possibly due to Galactic contamination. The field of view is 31.°9.

in colder regions) from 545 GHz (or 857 GHz) to 217 GHz and below.

3.2. Final SZ map

After building the individual SZ effect maps at 70, 100, and 143 GHZ from Eq. (3), these maps are combined with weights proportional to the inverse of their variance to produce a single SZ effect map. The weighted map is converted to Compton parameter units taking into account the *Planck* instrumental response (i.e., the convolution of the SZ spectrum in the non-relativistic case with the bandpass of *Planck*) in each band and the band differences involved in defining M^{c}_{217}, D_T, and SZ_ν, as described above.

The individual SZ effect maps at 70, 100, and 143 GHz are shown in Fig. 4. Virgo is clearly seen in all of them as an extended source a little below the centre of the image. Other clusters can also be seen in the same field of view, with Coma being the most prominent in the top part of the images. Bright radio and infrared sources (including the superluminous M 87 at the centre of Virgo) and the central part of Coma have been masked, together with small very bright regions of the Galaxy. The mask is built after defining a threshold in the SZ map where the brightest features (bright clusters like Coma and bright compact Galactic regions which correspond to the regions with the highest optical depth in Fig. 2) are masked out. The maps presented in Fig. 4 have been smoothed to a resolution of 1.°5 (FWHM) in order to better appreciate the extent of the signal around Virgo and reduce the noise. The field of view is 31.°9 across. Some artefacts can be seen in the maps, especially at 143 GHz, where vertical stripes can be clearly appreciated over the entire field of view. We apply a simple technique to reduce the negative impact of these stripes. Details of the stripe removal process are given in Appendix A. After the stripe removal, the individual SZ maps (at 70, 100 and 143 GHz) are combined together as described above to produce the final SZ map (see Figs. 5 and 6).

3.3. Galactic residuals

Among the possible systematics affecting our results, the Galaxy is probably the dominant one. Unknown variations in the dust temperature and spectral index, especially in diffuse cold regions with low emissivity at infrared frequencies, may leave residuals that could be mistaken for, or contaminate, the SZ effect map. A simple test can be performed to identify regions where the SZ map is more likely to be contaminated by Galactic residuals. We multiply the mean-subtracted maps of the SZ by an estimate of the dust in order to highlight potential Galactic contaminants. The result is shown in Fig. 7. We build the dust template as the difference between the 353 GHz and 217 GHz bands (see Sect. 3.1). This choice guarantees that the dust template is as close as possible to the dust components used to build the SZ map (70−217 GHz), thus minimizing the bias due to deviations from the mean of the dust temperature and spectral index observed near the Virgo cluster (see Fig. 2). A small amount of SZ effect (compared with the amplitude of the Galaxy) is expected to contribute to this dust template but its significance is small for our purposes. We multiply the mean-subtracted SZ map and dust template (both at a common resolution of 15′) and later we degrade this map to a resolution of 1.°5. The smoothing kernel locally integrates the correlation between the two maps, cancelling out the signal in those regions with small correlation and boosting the signal in those regions with more correlation (on scales comparable to the smoothing kernel). The sequence of dark and bright spots in Fig. 7, which are aligned in the diagonal arc (going from the bottom-left to the top-right) identify a region where the SZ map is most likely to be contaminated by Galactic residuals. The brightest spot in this arc corresponds to a 6σ deviation, where the Galaxy removal has over-subtracted the Galaxy (mimicking the SZ effect decrement), while the darker regions

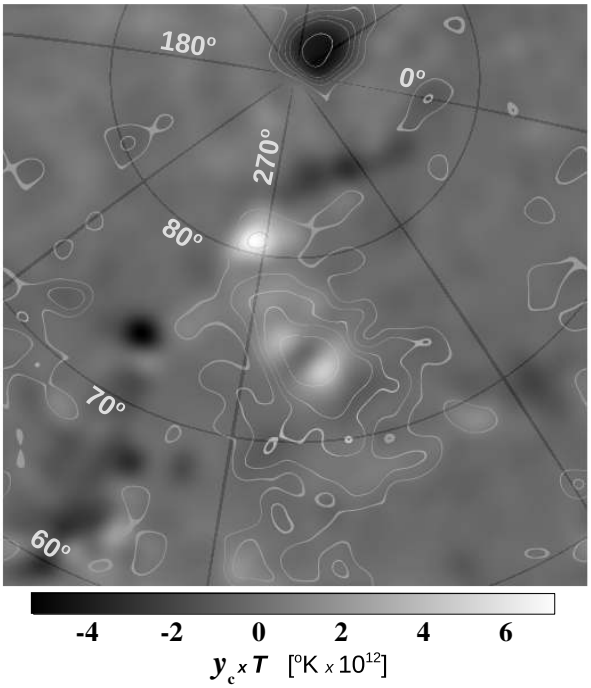

Fig. 7. Map showing the correlation between the SZ map and the dust map. The brighter areas show the regions where the correlation between the two maps is positive, while the darker areas show areas with anti-correlation. Overlaid are the same SZ effect contours as in Fig. 6. The units are arbitrary and re-scaled by a factor of 10^{12}, but correspond to the dimensionless Compton parameter times temperature.

in the arc mark the regions where the Galaxy removal has not subtracted enough Galactic signal. Note how the arc-like diagonal feature seen in Fig. 7 (extending from $\ell \approx 250°, b \approx 60°$ to $\ell \approx 330°, b \approx 85°$) traces the cold Galactic regions (see left panel in Fig. 2). Dark regions in this map can be seen also as areas where the SZ effect and Galactic emission are anticorrelated, while lighter regions mark the areas where both signals are correlated. The dark blob at the position of Coma (anti-correlation) is produced by the lack of Galactic signal in this region combined with a strong SZ signal. Around the centre of Virgo, the correlation indicates that both maps, the SZ map and the Galactic emission map, have positive signal.

This simple test suggests that the bright 6σ blob observed in the SZ map in the northern part of Virgo (and marked with a small light-blue circle in Fig. 6) may be a Galactic residual. We henceforth mask this area in our analysis to avoid this possible contamination. The remaining area of Virgo, on the other hand, seems to be free of significant Galactic residuals.

4. Complementing *Planck* with X-ray data

The combination of SZ effect and X-ray data improves the constraints on the plasma properties, as shown in Planck Collaboration Int. V (2013). We combine several X-ray data sets with *Planck* to extract additional information about the cluster gas distribution. Among other experiments, Virgo has been observed by ROSAT, *XMM-Newton*, *Chandra*, and *Suzaku*. Each of these instruments offers different advantages. The ROSAT All Sky Survey (RASS) is to date the most detailed all-sky map of the X-ray Universe at low energies (1–2 keV) and the only experiment that covers the entire cluster. In RASS data, Virgo is the biggest single extragalactic object in the sky, in terms of its angular size.

4.1. X-ray data

The X-ray analysis on large scales is based on the maps of the diffuse background from the RASS[2]. RASS data is presented in a set of maps and bands (0.1−2 keV). We focus on the diffuse ROSAT maps, in the R6 + R7 band (or ≈0.7−2 keV, Snowden et al. 1997) where the most prominent point sources (AGN) above 0.02 counts s^{-1} are masked. Above this threshold, there are still some sources that were not completely removed from the data, but their impact in the diffuse X-ray maps is small. The low-energy bands are more contaminated by local emission (the Local Bubble and the Milky Way). This band R6 + R7 is more advantageous in terms of instrumental response, background contamination, and cluster versus AGN emission. The pixel size of the diffuse RASS maps is 12′ and the units are counts s^{-1} $arcmin^{-2}$. The large pixel size (a downgrade from the original pixel size of the PSPC camera) is not an obstacle for our purposes and it is comparable to the resolution of our SZ effect map (15′).

We repixelize the diffuse all-sky maps from ROSAT R6+R7 band (with a native pixel size of 12′ × 12′) using `HEALPix`[3] at the resolution level $N_{\rm side} = 2048$. Although the R6 + R7 band is the best compromise between Galactic and AGN contamination, it still contains Galactic emission that affects the Virgo region. In particular, the North Galactic Spur reaches the vicinity of the Virgo cluster. We mask this region from our analysis of the X-ray data (when computing the profiles).

In addition to ROSAT we use results from two other observatories. *XMM-Newton* data have been used recently by U11 to study the X-ray emission in Virgo out to the virial radius. Although the *XMM-Newton* data used in that work covers only a linear slice through a small fraction of the cluster area, it is of great interest since it constrains the gas density and temperature out to large radii. Figure 8 shows the sector used in this *XMM-Newton* study superimposed on the SZ effect and RASS maps.

At higher-resolution, *Chandra* data have been used by G04 to study in detail the innermost region of Virgo, producing tight constraints on both electron density and temperature. Figure 9 shows these two data sets compared with models for the electron density. In addition, we also show a model that is built from the combination of the two models (solid line), which we refer to as the "hybrid" model. The temperature profile is shown in Fig. 10; the solid line shows the hybrid model for the temperature, which we discuss in Sect. 6.

4.2. X-ray to SZ ratio

In Fig. 11 we present the ratio of the X-ray flux, $S_{\rm X}$, to the Compton parameter map of Virgo, $y_{\rm c}$, (the Coma and Leo clusters are also seen in the map). It shows the ratio of smoothed versions (Gaussian kernel with $FWHM = 1.5°$) of the X-ray and the y-maps for regions where the smoothed y-map S/N is above 1.5. The increase of the ratio at the edge of the contour region is mostly driven by the decrease in the $y_{\rm c}$ signal since the X-ray emission is approximately constant at large radii (i.e., it reaches the background level). This map shows crudely (but free

[2] `http://www.xray.mpe.mpg.de/rosat/survey/sxrb/12/ass.html`
[3] Górski et al. (2005), `http://healpix.sf.net`

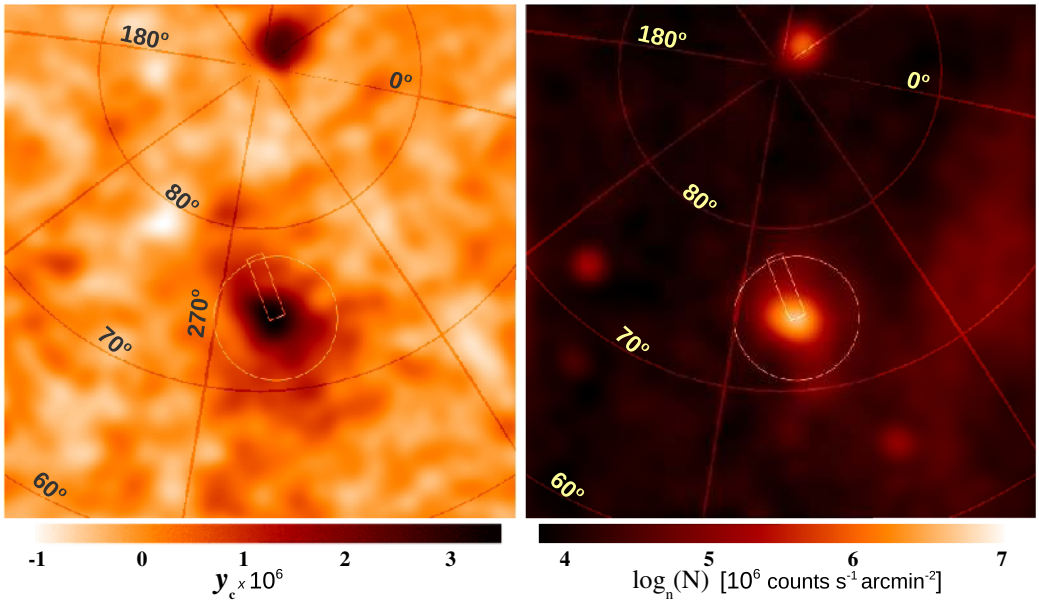

Fig. 8. *Left*: SZ map (stripe-reduced version) in units of the Compton parameter. *Right*: ROSAT All Sky Survey map in Logarithmic scale (in units of 10^6 counts s^{-1} arcmin^{-2}). We indicate the sector (rectangular region) where *XMM-Newton* pointings were used by Urban et al. (2011) to derive the electron density and temperature up to the virial radius (circle).

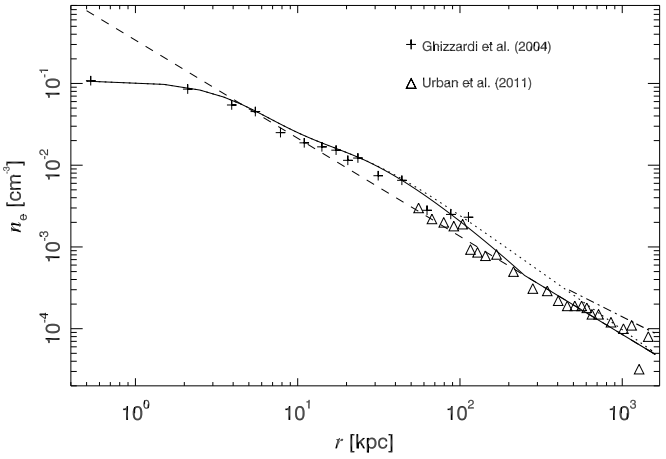

Fig. 9. Electron density profile of Virgo derived from *Chandra* and *XMM-Newton* data. The dotted and dashed lines correspond to the fits derived by G04 and U11, while the solid line shows the hybrid model adopted in this paper, combining the features from the G04 and U11 models. The dot-dashed line shows an alternative model that extends the G04 model beyond 500 kpc with an r^{-1} power law. Error bars are omitted for clarity.

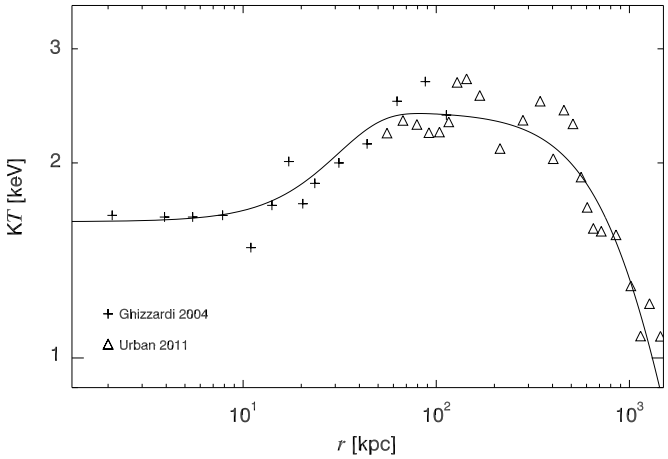

Fig. 10. Temperature profile of Virgo derived from *Chandra* and *XMM-Newton* data. The solid line shows the hybrid model adopted in this paper, see Eq. (6).

from any geometrical assumptions) the electron density profile of the clusters in the plane of the sky. This can be seen from

$$\frac{S_X}{y_c}(\theta) \propto \frac{\int \mathrm{d}l\, n_e^2(\theta)\, \Lambda(k_B T(\theta))}{\int \mathrm{d}l\, n_e(\theta)\, k_B T(\theta)}$$

$$= \left. \frac{\int \mathrm{d}y_c(\theta)\, (n_e\, \Lambda(k_B T)/k_B T)(\theta)}{\int \mathrm{d}y_c(\theta)} \right|_{\mathrm{d}y_c(\theta) \propto n_e(\theta)\, k_B T(\theta)\, \mathrm{d}z}$$

$$= \langle n_e\, \Lambda(k_B T)/(k_B T) \rangle_{y_c}(\theta), \quad (5)$$

where $\Lambda(k_B T)$ is the temperature dependence of the X-ray emission in the observed band and θ is the direction of the line of sight. For an isothermal cluster, this map shows the y_c-weighted (or equivalently pressure-weighted) electron density along each line of sight. Since the temperature within the cluster gas varies at most by a factor of a few, it only weakly modulates the X/y_c map, in comparison to the electron density, which exhibits a much steeper variation. Furthermore, since the cluster pressure profile is highly structured and is typically larger in the plane of the sky going through the cluster center, then the X/y_c-map predominantly shows the electron density within this plane. Although this interpretation is certainly complicated by temperature structures in the cluster gas (or errors in the X-ray and more importantly in the SZ map), as well as by the remaining impact of the pressure weighting, the X/y_c-map provides a simple and robust way to obtain some insights into the structure of the cluster plasma. In Sect. 7 we study the distribution of the plasma beyond the virial radius in more detail.

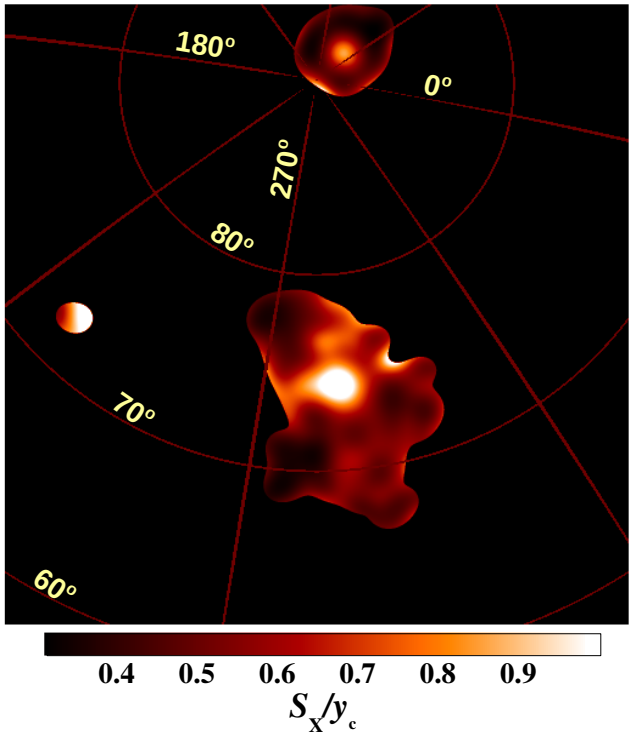

Fig. 11. Ratio between ROSAT and *Planck* data (smoothed to 1°.5). The ratio S_X/y_c is defined only in regions with sufficient SZ signal (the smoothed signal is bigger than 1.5 times the dispersion of the map). Three clusters can be distinguished in this plot, Coma in the north, Virgo in the centre, and Leo (with a much smaller S/N) in the east. The ratio is normalized to 1 at the maximum.

5. Electron density and temperature models

To model the electron density, we use two models found in the literature and derived from *Chandra* and *XMM-Newton* data. The first one is a model derived by G04 (Eqs. (2) and (3) in that paper), which describes the data in the central $r < 120$ kpc region. This model does not account for the cluster emission in the outer regions of Virgo, but should be an accurate description of the central part. For the outer regions we consider a second approach that corresponds to the sector model derived by U11, which extends the profile up to the virial radius (≈1 Mpc).

In addition to these two models, in some later parts of this paper we use a hybrid model that combines the features from G04 and U11. Following U11, we model the electron density in the outer region as a power law,

$$n_e(r) = \frac{8.5 \times 10^{-5}}{(r/\mathrm{Mpc})^{1.2}}\ \mathrm{cm}^{-3}. \quad (6)$$

This power law is shown as a dashed line in Fig. 9. The inner region is described by the model of G04, while the intermediate (approximately 30−250 kpc) region between the G04 and U11 estimates is linearly interpolated between the G04 and U11 models. This hybrid model is shown as a solid line in Fig. 9. Alternatively, in Sect. 7, we use an additional model that assumes the density profile from G04 up to $r = 500$ kpc and beyond this radius the density goes like an r^{-1} power law. This is shown as the dot-dashed line in Fig. 9. We should note however that due to the masking of the central M 87 region of Virgo, the results from the hybrid model are very similar to the results derived using the U11 model.

For the temperature profile, we use a model that combines the features from G04 and U11. This model is shown as a solid line in Fig. 10 and is given by

$$T(r) = \frac{2.4 - 0.77 \times \mathrm{e}^{-(r/\mathrm{Mpc})^2/(2\sigma_r^2)}}{1 + [0.9 \times (r/\mathrm{Mpc})]^2}\ \mathrm{keV}, \quad (7)$$

with $\sigma_r = 23.7$ kpc.

At large radii, the model shown in Eq. (7) drops quickly. To avoid unphysically low temperatures we set a lower limit for the temperature at 1 keV in the outer region ($r > 1$ Mpc), which is consistent with what is expected between R_{vir} and $2 \times R_{\mathrm{vir}}$, where the temperature is expected to change only by a small amount (Roncarelli et al. 2006; Burns et al. 2010). When modelling the cluster, we set a truncation radius at ≈8°.3.

5.1. Deprojected models

In addition to these models, and as an independent comparison, we derive our own pressure profile based on a sparse set of *XMM-Newton* pointings that irregularly sample a region of a few degrees around Virgo. For the X-ray analysis in Sect. 5.2 we have used data from the *XMM-Newton* public archive (see Table B.1 with ObsID). For the analysis of the *XMM-Newton* data we follow the procedure described by Churazov et al. (2003), which we briefly summarize here. The data are cleaned from flares using the count-rate of the combined MOS detectors above 10 keV. The steady component of the background is calculated from the data of blank field observations provided by the *XMM-Newton* SOC site[4]. The remaining variable background component is estimated using the mean flare spectrum shape (averaged over a large set of moderate and faint flares) and normalized using the observed spectrum between 11 and 12 keV. The sum of the steady and variable components in each observation is used as a total background in this observation. The image is built in the 0.5−2 keV band, background-subtracted and vignetting-corrected. For each observation a vignetting map is evaluated for the mean energy of the image, taking into account the offset of a given pixel from the pointing centre of the observation. The vignetting maps are multiplied by the corresponding exposure times and combined into a *vignetted* exposure mosaic. For the spectra we follow a slightly different route for the vignetting correction. Namely, for each event from the event-list we calculate the vignetting based on the event energy and offset from the pointing centre of a given observation. The spectra have been extracted in concentric annuli, centred on M 87, and increasing the radii logarithmically. Given the coverage of the outer regions with *XMM-Newton* only a fraction of each annulus is filled with data. For the vignetting calculation we used the information from the standard ancillary response files (see Sect. 2 in Churazov et al. 2003, for details). When the spectra are accumulated over a given region, the events corrected for this drop in efficiency are added together. Appropriate corrections are also applied to the background events and to errors associated with each spectral channel. The projected and deprojected spectra were fitted in `XSPEC` (Arnaud 1996) with the single temperature `APEC` model (Smith et al. 2001), fixing hydrogen column density at 2.5×10^{20} cm^{-2} and metallicity $Z = 0.5$ for the abundance table of Lodders (2003).

After the data are corrected, we use the sparse pointings to deproject the emissivity, assuming spherical symmetry (see Churazov et al. 2003). Prior to the deprojection all strong compact sources and few prominent Virgo galaxies are removed.

[4] http://xmm.esac.esa.int/

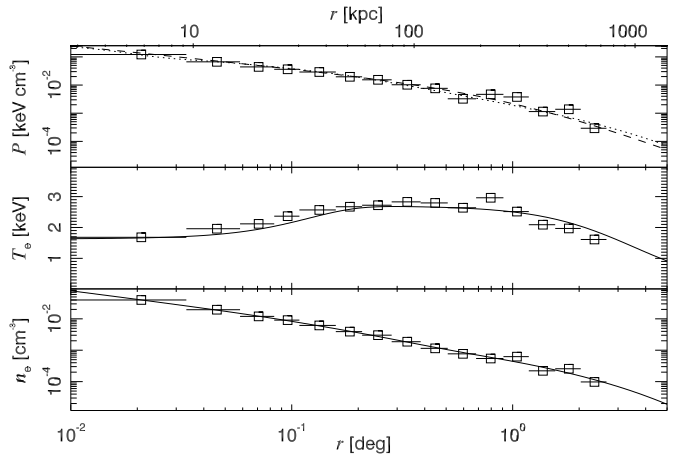

Fig. 12. Deprojected pressure (*top*) and electron density profiles (*bottom*) from the sparse *XMM-Newton* data. The *middle panel* shows the projected temperature (see text). The pressure (*top panel*) is compared with an Arnaud et al. (2010) profile (dotted line), which fits the data well within the virial radius. The solid curves (dotted curve in the case of the pressure) represent a simple analytical model that fits the derived temperature and electron density. The pressure predicted from the deprojection analysis (dotted curve) is compared with the observations in Fig. 14.

5.2. Derived profiles

In Fig. 12 we show the electron density, gas temperature, and pressure radial profiles. Notice that in the middle panel we show the projected values of the temperature (to avoid large scatter in the deprojected T values). The density and temperature radial profiles have been approximated with simple analytic functions, shown with black solid lines. The top panel of Fig. 12 shows the product of the analytic approximations for the density and temperature distributions (black curve). Also shown is a universal pressure profile (Arnaud et al. 2010, dotted line) with $P_0 = 3.5\,\mathrm{keV\,cm^{-3}}$, $c_{500} = 2.5$, $\gamma = 0.8$, $\alpha = 1.33$, and with the outer slope fixed to a shallow index, $\beta = 3.0$, using the form

$$P(x) = \frac{P_0}{(c_{500}\,x)^{\gamma}[1 + (c_{500}\,x)^{\alpha}]^{(\beta-\gamma)/\alpha}}, \quad (8)$$

with $x = r/r_{500}$. For this profile, we adopt the value $r_{500} = 770\,\mathrm{kpc}$ (with r_{500} the radius at which the enclosed overdensity is 500 times the critical density), derived from the X-ray derived temperature and cluster mass relation, T_X–M, from Vikhlinin et al. (2006) for $T_X \approx 2.3\,\mathrm{keV}$. A shallow outer slope, $\beta = 3.0$, is consistent with the SZ profile of Coma at large radii (Planck Collaboration Int. X 2013) and also with the SZ profile (at large radii) of stacked clusters (Planck Collaboration Int. V 2013).

We should emphasize again that the deprojection technique involves the assumption (probably erroneous in this case) that the cluster has spherical symmetry. The possible geometry of the cluster is discussed in Sect. 7.2. Also, the sparse coverage of the Virgo region by *XMM-Newton* is neither random nor systematic (except for the stripe to the north), but tends to concentrate on cluster member galaxies or prominent AGNs. These effects leave considerable uncertainty in the X-ray-based profiles.

6. Model fits to the data

It is interesting to compare the SZ signal with the predictions made by the models derived from X-ray data. We compare the data with the models by computing a "radial profile" (average signal in circular bins) and a "sector profile" (average signal along the sector shown in Fig. 8) for both the data and the models. The radial profile of the data is computed after smoothing both *Planck* and ROSAT data with a Gaussian, the final resolution after the smoothing being 15′ for both data sets. For the sector profile, we compute the profiles considering only the data contained in the rectangular region of Fig. 8 (but extending the rectangle towards the north-east). The extension of this region towards the north-east intersects the feature that is likely due to Galactic contamination in the SZ map (marked with a small light-blue circle in Fig. 6). This feature is clearly visible in Fig. 13 as a bump in the SZ sector profile at around 7°. In the X-ray profile from ROSAT, which extends beyond the region studied by U11, there is no evidence for a similar feature, supporting the hypothesis that this feature is a cold Galactic residual in the SZ map.

The Compton and X-ray profiles for the G04 and hybrid models (for n_e and T), are computed assuming spherical symmetry and are truncated at 10° (or 3.7 Mpc). Virgo is assumed to be at a distance of 21.46 Mpc ($z = 0.005$) and we adopt a `MeKal` model with metallicity $Z = 0.3$ (metal abundances are taken from Anders & Grevesse 1989) and HI column density $n_H = 0.0207 \times 10^{22}\,\mathrm{cm^{-2}}$ (Kalberla et al. 2005). This model is convolved with the instrumental response of ROSAT using `XSPEC` at the desired energy range to produce the predicted count rate. We build projected 2D maps (SZ and X-ray) that are masked and smoothed with the same masks and smoothing kernels applied to the real data and described above.

Figure 13 shows the comparison between the data and the models. Errors in the profiles are discussed in more detail in Sect. 7. The X-ray radial profile is reproduced reasonably well at small radii by both models, with the model of G04 predicting more signal than the hybrid model. At $R > 2°$, both models overpredict the observed X-ray signal. This mismatch could be due to the lack of symmetry of the cluster and the fact that the model at large radii is derived from a single sector in the cluster that may not be representative of the circularly averaged signal at large radii. For the sector profile, the hybrid model fits the data better than the G04 model in the intermediate region ($r \approx 2° \approx 600$ kpc). The G04 model beyond 200 kpc (corresponding to about 0.°6) has a higher electron density than the U11 model (see Fig. 9), which results in more predicted X-rays than observed in the sector region at around 2°. When comparing the models with the SZ effect data, the differences are more evident. In both the radial and sector profiles (bottom panels in Fig. 13), the hybrid model does not describe the central region as well as the G04 model, which gives an excellent fit to the core region in both cases. In the outer regions both models converge and perform similarly in the radial and sector profiles.

Better S/N in the SZ data can be obtained by binning the SZ signal in wider radial bins. Figure 14 shows the Compton parameter, y_c, from *Planck* in wide radial bins (33′ wide). The errors are computed as the dispersion of the individual radial bins in each wide bin (see Sect. 7.1 for more details). Also shown is the signal predicted by the shallow models described in Sect. 5, namely the G04 model (green line) and the hybrid model (light blue line). It is important to emphasize that these models are generally constrained with data up to around 4°, so the models beyond this point are extrapolations. In addition, the shallow y_c profiles ($\beta = 3$) inferred from the deprojection analysis (from the sparse X-ray data) are shown as red curves. The solid one assumes that M 87 is at a distance of $D = 16$ Mpc, while the dashed line assumes $D = 21$ Mpc. For comparison the purple solid line corresponds to the Arnaud et al. (2010) profile with the standard

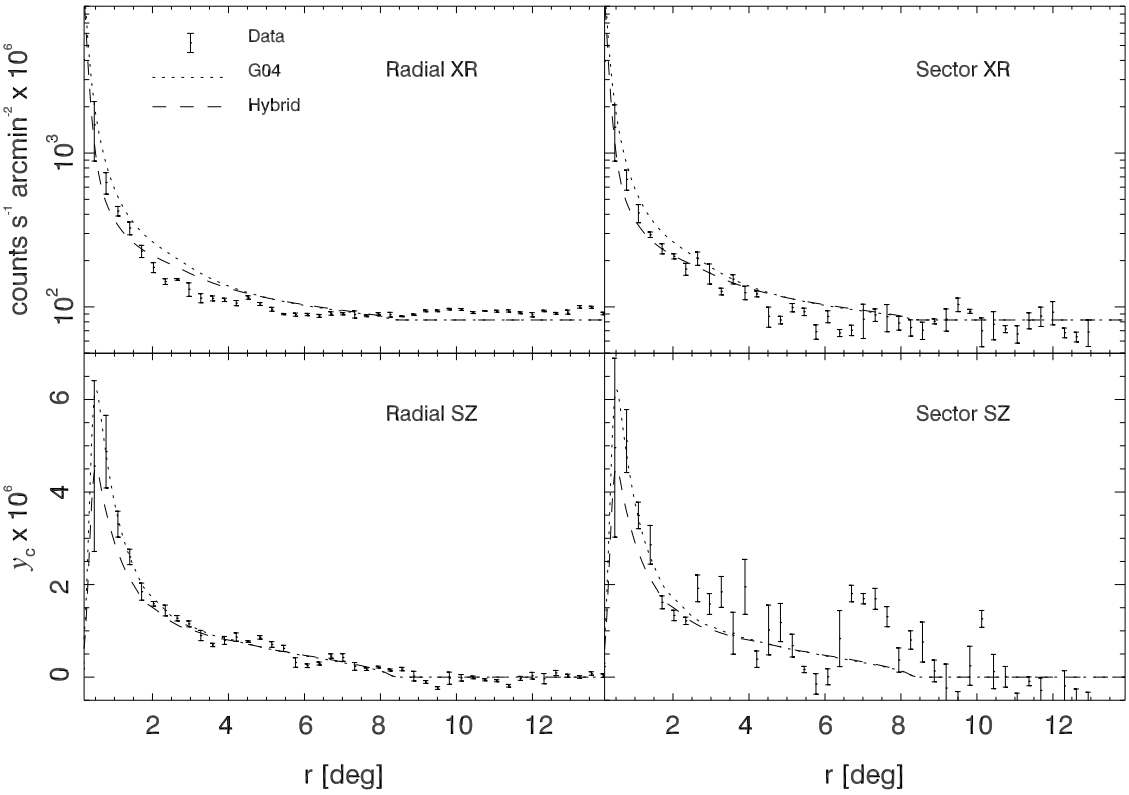

Fig. 13. *Planck* SZ and ROSAT X-ray profiles compared with the G04 and hybrid models. The two plots on the *left* correspond to the radial profile and the two plots on the *right* correspond to the sector profile. For the sector profile, the SZ feature at 7° is not masked in order to highlight its effect.

set of parameters; $P_0 = 6.41$ keV/cm^3, $c_{500} = 1.81$, $\gamma = 0.31$, $\alpha = 1.33$, and $\beta = 4.13$ (Planck Collaboration Int. V 2013). Both versions of the Arnaud et al. (2010) profiles (shallow index $\beta = 3.0$ and standard values) give a reasonable description to the observed profile in the central region (up to around 2.5°, corresponding to r_{500}) but underpredict the observed (SZ) pressure at the virial radius (roughly 4°) and beyond, with the shallow profile ($\beta = 3.0$) reproducing the data better.

An indication that the Arnaud et al. (2010) profile (with its original parameters) derived from X-ray data underpredicts the pressure at large radii was also found in Planck Collaboration Int. V (2013), where a joint X-ray and SZ analysis concluded that shallower profiles ($\beta < 4.5$ and $\beta < 4$ for non cool-core clusters, respectively) are favoured. A similar conclusion was obtained in the *Planck* analysis of the Coma cluster (Planck Collaboration Int. X 2013). In the case of Coma, it was found that even shallower pressure profiles ($\beta \approx 3$) were required to fit the SZ signal at large radii (Planck Collaboration Int. X 2013). The Virgo cluster allows us to extend the radii even further and points in the direction of an increased shallowness at the largest radii. This is expected at some point, since the y_c profile should converge to the average y_c for sufficiently large radii. If reservoirs of ionized gas concentrate around the clusters (as shown in Fig. 1) we should expect a gradual flattening of the profile as the distance to the cluster centre increases.

Another interesting result is the fact that the G04 model seems to agree better in the central region, while both models agree well with the observations in the most distant regions. The SZ signal extends beyond twice the virial radius suggesting the presence of warm gas around the cluster. The signal in the outer regions is studied in more detail in Sect. 7. Finally, the two profiles derived from the sparse *XMM-Newton* pointings show some dependence on the assumed distance to Virgo. This will be discussed in more detail in Sect. 7.3.

7. Gas beyond the virial radius

Figure 6 shows how the SZ signal extends beyond the virial radius. This picture is quite different for X-ray observations, where the emission vanishes soon after the virial radius. The lack of X-ray signal in regions where there is still SZ signal can be used to constrain the properties of the plasma in these regions. Intuitively, a boost in the SZ signal from a low-density plasma can be produced (without a significant X-ray counterpart) if the plasma extends along the line of sight as a low-density medium and/or its temperature remains sufficiently high (1 keV or above). In the previous section, a preliminary comparison between the SZ and X-ray profiles was presented. In this section we focus on the signal at the outskirts of the cluster, where the gas properties are poorly constrained.

We study the signal in the outskirts of Virgo in two different ways. First, we stack the signal in wide radial circular bins around the central point (each radial bin is an annulus with an inner and outer radius; the difference between these two radii defines the width of the bin). We refer to these bins as "wide-radial bins". Second, we account for the lack of symmetry in Virgo and define non-symmetric bins that trace the S/N of the SZ map (see Fig. 16). We refer to these bins as "contour-region bins".

7.1. Wide-radial bins

In order to maximize the S/N in a radial bin we consider wide bins with a 33′ difference between the inner and outer radius of each bin (or 30 pixels wide in our native maps). In each wide

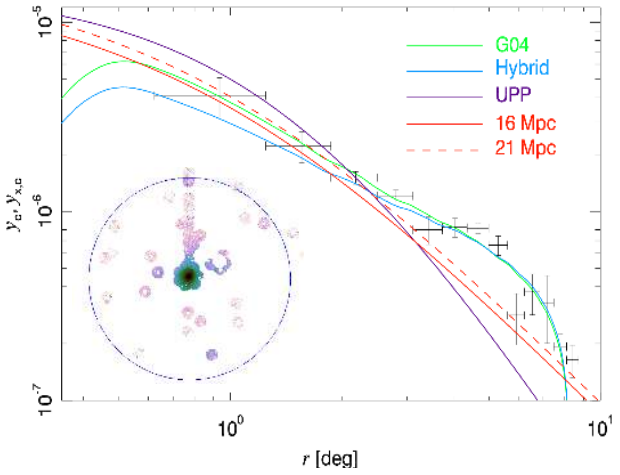

Fig. 14. Binned pressure profiles derived for Virgo (black points with errors). The light-blue line shows the prediction from the hybrid model and the green line shows the prediction from the G04 model. Both models decrease at small radii due to the point source mask in *Planck* data, which is also applied to the simulated data (models). The dashed and solid red curves show the deprojected pressure from X-ray data assuming a universal shallow profile (with outer slope $\beta = 3$, see text) for a Virgo distance of 21 Mpc and 16 Mpc, respectively. As a comparison we show as a solid purple line the standard (steeper) Arnaud et al. (2010) profile ($\beta = 4.13$) for the case where the distance is set to 16 Mpc. The sparse sampling by *XMM-Newton* used to infer the deprojected pressure is shown in the bottom left with the circle marking the virial radius. The stripe with *XMM-Newton* pointings used in U11 is seen clearly in the vertical direction.

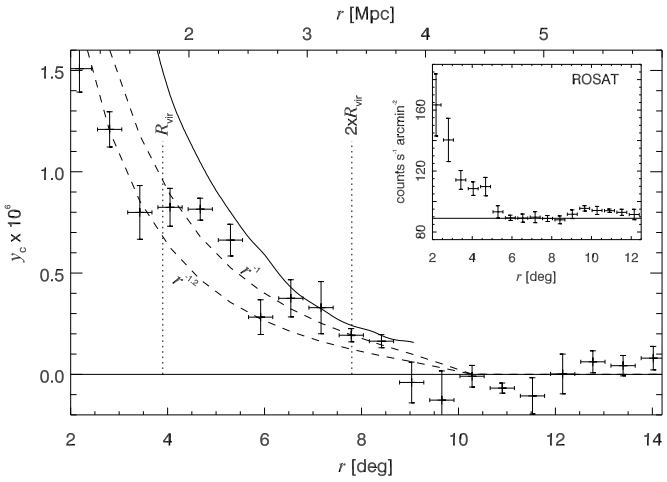

Fig. 15. Binned radial y_c profile of Virgo outskirts. The bins are 30 pixels wide (or equivalently 33′, or 230 kpc). The two dashed lines correspond to the expected signal from two analytical models where the electron density beyond 0.5 Mpc falls as r^{-1} or $r^{-1.2}$. At $r = 0.5$ Mpc the model is normalized to the electron density given by G04 at that distance. At distances smaller than 0.5 Mpc the electron density follows the model of G04. The solid line shows the profile of the simulated Virgo cluster. The *inset* shows the corresponding profile in the ROSAT map using the same bins (with units the same as in Fig. 13).

bin we compute the mean and dispersion of the individual profiles (the individual profiles are computed in a ring of width 1 pixel). These profiles are computed considering only regions in the SZ map that are not masked by the point source or Galactic mask. The Galactic mask also excludes from our analysis the region in the north part of Virgo (small circle in Fig. 6 or 6σ fluctuation in Fig. 7) that is likely contaminated by Galactic dust (see Sect. 3.3 above). The resulting binned profile, with its corresponding dispersion, is shown in Fig. 15. We should emphasize that the error bars shown in Fig. 15 represent the dispersion of the individual 1 pixel wide radial bins in the 30 pixel wide ring. This dispersion accounts for the correlated nature of the noise and the intrinsic variability of the profile in the 33′ angular range. The binned profile shows an excess with respect to the background out to at least twice the virial radius (and possibly beyond).

For comparison, we also show in the inset the profile from ROSAT using the same radial bins. A first conclusion is that the SZ signal seems to extend significantly farther than could be inferred from X-ray data alone, directly pointing to the presence of previously undetected plasma at large radii. Also, interestingly, the average profile is consistent with the extrapolation of the U11 profile ($\propto r^{-1.2}$). For comparison, we also show as a dashed line in Fig. 15 the expected signal for a shallower ($r^{-1.0}$) profile. This model assumes, for the electron density, the G04 model up to $r = 500$ kpc and an $r^{-1.0}$ profile beyond this point. The $r^{-1.0}$ power law part of this model is shown in Fig. 9 as a dot-dashed line. The shallow SZ profile beyond the virial radius is significantly different from the average profile observed in the outer radii of other *Planck* clusters (Planck Collaboration Int. V 2013), where steeper profiles closer to r^{-3} or even $r^{-4.5}$ are preferred beyond the virial radius (assuming a nearly isothermal profile at large radii). The two models shown in Fig. 15 (dashed lines) are truncated at a relatively large radius (10° or about 3.7 Mpc at the distance of the cluster). The effect of the truncation radius can be noticed beyond a distance of about 8° from the centre, where both models start to converge towards zero.

The shallowness of the profile of Virgo in the outermost regions ($r > R_{vir}$) may be due to the presence of significant amounts of plasma beyond the virial radius. The increased sensitivity of our analysis (due to the big area being integrated) allows us to explore the outskirts of a cluster to distances never examined before. For instance, the bin at a distance of about 4° from the centre integrates the signal over a total area of roughly 15 deg^2, and the bin at about 8° integrates a remarkable total area of 30 deg^2, reducing the noise levels to an unprecedentedly low value. The profile at large radii may be sensitive to the presence of the elusive WHIM, which is expected to contribute at the 1-μK level around Virgo (Fujimoto et al. 2004; Diego & Ascasibar 2008). A reassuring result from Fig. 15 is the excellent agreement in the outer region ($r \approx 2\,R_{vir}$) of the binned profile with the profile from the simulated cluster shown in Fig. 1 (solid line in Fig. 15). At smaller radii, the simulation systematically overpredicts the observed signal, which may be a consequence of insufficient modelling of the ongoing physical processes in the central region of the cluster (in particular a powerful AGN like M 87 that may not be properly included in this simulation although the simulation does incorporate feedback from AGN activity).

7.2. Contour-region bins

The previous section presented results about the SZ cluster up to twice the virial radius. However, we made the assumption that the cluster is spherical when comparing this signal with the models, while clearly Virgo exhibits a non-spherical morphology. In order to test the possibility of constraining the plasma properties in the outskirts of the cluster independently of the geometry of the cluster, we divide the cluster into different regions according to the S/N in the SZ map shown in Fig. 16. These regions are defined in terms of the dispersion of the smoothed

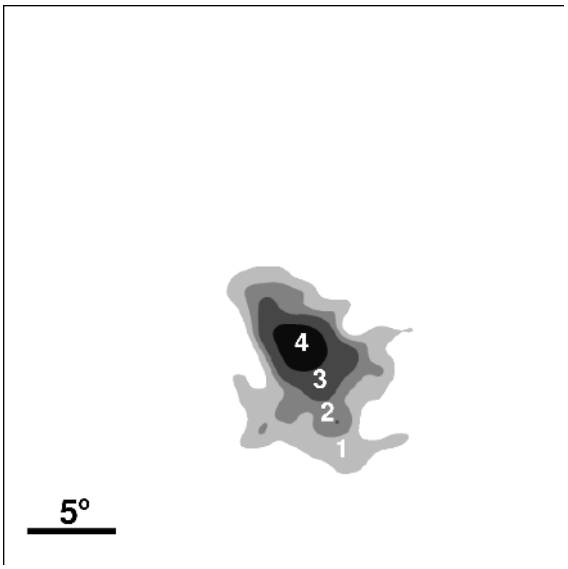

Fig. 16. Four regions defined by the S/N of the SZ effect. From lightest to darkest, $S/N \in [2,3)$, $S/N \in [3,4)$, $S/N \in [4,7)$, and $S/N > 7$. Note that the likely spurious structure in the northern part of Virgo is not included in our analysis. See Fig. 6 to see the same contours in relation to the SZ signal.

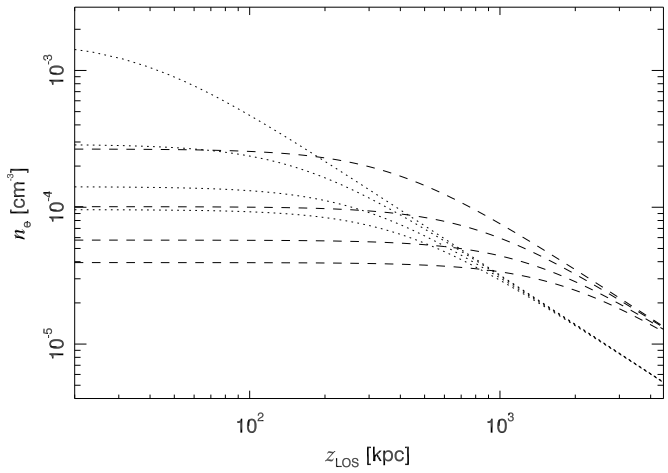

Fig. 17. Model of the electron density along the line of sight coordinate (z_{LOS}) for the four different regions and for two sets of models. The dashed lines are for a spherical model, while the dotted lines are for an ellipsoidal model. For each group and from bottom to top, we show the cases for regions 1–4.

SZ map. Region 1 corresponds to the area where the signal in the smoothed map is between 2 and 3 times the dispersion of the smoothed map (σ_s). Region 2 is for the signals between 3 and $4\,\sigma_s$, region 3 for signals between 4 and $7\,\sigma_s$, and region 4 for signals bigger than $7\,\sigma_s$. We retain only the regions that are associated with the cluster and, as in the previous section, we exclude the clump in the northern part of the Virgo cluster that is due to a Galactic residual (as discussed in Sect. 3.3). The regions shown in Fig. 16, especially the outer ones, can be seen as areas of the cluster with similar optical depth (assuming the temperature does not change much, which should be a better assumption along lines of sight that do not cross the centre of the cluster). This is a consequence of the linear dependence of the SZ effect on the electron density and the relatively small change in the temperature. Although the regions are defined after smoothing the SZ map with a $1.^\circ5$ Gaussian kernel, we use the SZ map at the original $15'$ resolution. To model each region we adopt a simple approach based on the observational X-ray constraints discussed above. The temperature is taken directly from the hybrid model discussed above (see Eq. (7)). For the electron density, we adopt a law $n_e = Ar^{-1.2}$ like in U11, and assume that each region corresponds to the signal along a line of sight (z_{LOS}) at an angular distance, or impact parameter b, from the centre (that is, $r = (z_{LOS}^2 + b^2)^{1/2}$). Both A and b are adjusted to fit the SZ and X-ray data, but with the constraint that the normalization, A, must take the same value for all the regions (to guarantee continuity in the electron density), while the impact parameter, b, is adjusted for each region in order to simultaneously reproduce the observed mean SZ and X-ray signal in each region, where the observed mean signal is defined as the total signal in a region divided by the number of pixels.

We parameterize the electron density as a function of the impact parameter, b, as

$$n_e = \frac{A}{\left(b^2 + z_{LOS}^2\right)^{1.2/2}}, \quad (9)$$

where the coordinate z_{LOS} is integrated along the line of sight. In the above expression both b and z_{LOS} are given in Mpc when A takes the values of Table 1. Figure 17 shows the electron density profile used in each region along the line of sight. We consider two scenarios. In the first one (dashed lines in Fig. 17) we consider the cluster to have a spherically symmetric structure and that the U11 $r^{-1.2}$ estimation of the density profile is valid for the entire cluster (with the same normalization as in U11). In that case, the effective impact parameter, b, in Eq. (9) should be close to the average radius in a given region. We call this case the "spherical-like" model. In the second scenario, (dotted lines in Fig. 17) we assume a more realistic model where the spherical symmetry is not required. We still impose the constraint that, along a particular line of sight, the density has to follow an $r^{-1.2}$ law, but we relax the conditions on both the normalization, A, and impact parameter, b (although A is still forced to take the same value for all sectors). Letting the impact parameter take values that differ significantly from the average radius in a given region is similar to allowing the gas distribution to contract or expand along the line of sight in relation to the spherical distribution. We refer to this case as the "ellipsoid" model. Values of b significantly greater than the average radius in a region would correspond to density profiles that are more elongated along the line of sight (oblate). On the other hand, values of b smaller than the average radius would correspond to a profile that has contracted along the line of sight in relation to the spherical case (prolate). The parameters from Eq. (9) derived from our fit in the spherical-like and ellipsoid models are shown in Table 1. The models corresponding to these parameters are shown in Fig. 17. The last two columns of Table 1 contain the estimated mass of the gas in each region for two assumptions about the truncation radius, defined as the maximum radius out to which we integrate the SZ or X-ray signals. These masses are derived adopting the non-spherical distribution of Virgo as follows. Given the model for the gas density along the line of sight (Eq. (9)), the projected mass per pixel is computed for a single pixel in a given region and this mass is later multiplied by the number of pixels contained in that region. It is interesting to compare the masses for the two models. When the truncation radius is 2.5 Mpc, the gas mass per region is very similar in both models, with the ellipsoid model being slightly more massive. The situation is reversed

Table 1. Parameters of the electron density profile in Eq. (9) for the different regions and for two types of model.

Symmetry	Region	A [10^{-5} cm^{-3}]	b [kpc]	$M_{\rm gas}(r < 5\,{\rm Mpc})$ [$10^{13}\,M_\odot$]	$M_{\rm gas}(r < 2.5\,{\rm Mpc})$ [$10^{13}\,M_\odot$]
Spheroidal	1	8.5	1841	2.9	1.5
	2	8.5	1343	3.6	2.4
	3	8.5	840	4.8	3.6
	4	8.5	374	7.0	5.9
Ellipsoidal	1	3.2	400	2.7	2.2
	2	3.2	290	3.0	2.6
	3	3.2	160	3.8	3.4
	4	3.2	37	6.3	5.9

Notes. The first four rows are for the spherical model and the last four rows are for the ellipsoid model. The parameter b in the spherical model corresponds to the average radius of a given region. The amplitude A for this model is taken from the U11 model. The parameters A and b in the ellipsoid model have been adjusted to simultaneously fit the SZ and X-ray data. The gas masses are computed for two different truncation radii, 2.5 Mpc and 5 Mpc.

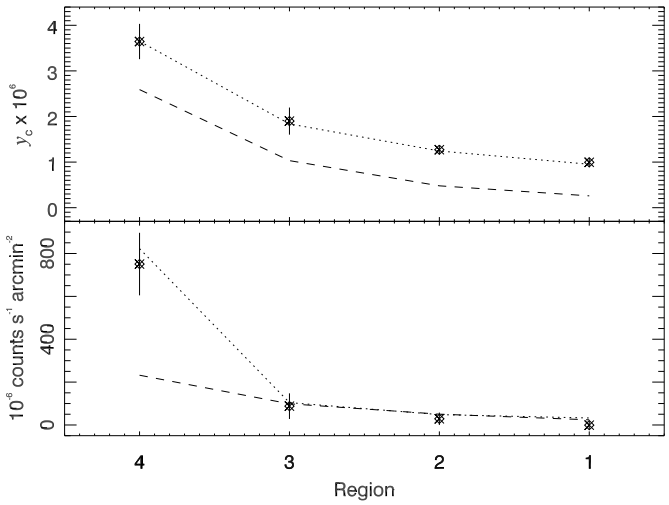

Fig. 18. Mean signal (from the 15′ resolution maps) in each of the four regions shown in Fig. 16 (asterisks with error bars) compared with the predicted signal from analytical models. The models are shown in Fig. 17, as a dashed line for the spherical model and dotted line for the ellipsoidal model. The error bars are the dispersion in each region of the 1°.5 smoothed maps.

if the profiles are truncated at 5 Mpc with the spherical model having more mass in this case. This is a direct consequence of the higher density of the spherical model at $r > 1$ Mpc.

The predicted mean SZ and X-ray signal in each region is shown in Fig. 18 (as lines) compared with the actual measurement (symbols with error bars). Both models generally agree well with the X-ray data in regions 1–3. Less attention should be paid to the fit in region 4 (containing the centre of the cluster), since we are approximating all lines of sight in a sector by a single impact parameter. This approximation is a particularly bad one when the line of sight lies close to the centre (impact parameter $b \approx 0$). The models in this region are not expected to reproduce the data accurately, especially for the X-rays (due to the strong dependency with $n_{\rm e}^2$), since both models assume an impact parameter that misses the central cusp. For the SZ effect, the spherical model (which reproduces well the circularly averaged profile, as shown in the previous section) fails to reproduce the observed signal in all regions. This highlights the lack of symmetry of Virgo and the importance of considering non-spherical models when trying to reproduce the observations. When allowing the normalization A and the impact parameter b to change in order to accommodate both SZ and X-ray data, we find that models that have smaller impact parameters, i.e., that concentrate the gas near the sky plane of the cluster (where the sky plane is defined as the plane perpendicular to the line of sight at Virgo's distance), are able to reproduce both SZ and X-ray region profiles simultaneously. A prolate model, where the axis of symmetry (the longest axis in the ellipsoid) is in the cluster plane (perpendicular to the line of sight), would be consistent with this picture. Our results disfavour oblate models, where the longest axis is parallel to the line of sight, since this would correspond to a much larger impact parameter b. This result is consistent with simulations and observations that conclude that clusters prefer to adopt prolate distributions (Cooray 2000; Sereno et al. 2006; Despali et al. 2014).

The increase in SZ signal when going from a spherical model to a prolate model (with approximately the same amount of gas in both models) can be understood if we realize that the prolate model concentrates more gas closer to the cluster centre, where the temperature is higher, hence increasing the pressure.

There is a relatively small change between the predictions of the spheroidal and ellipsoidal models for the X-ray emission. This may be due in part to the dependence on $n_{\rm e}^2$. However, we can see in Fig. 17, how a relative compensation in the density between the central and outer regions may be the reason for the small change between the spherical and ellipsoid models. While the spherical model has a higher density at large radii, at small distances from the cluster plane the ellipsoid model has more density than the spherical model. Even though the range of distances where the ellipsoid model is denser than the spherical model is smaller, the X-ray surface brightness gets boosted by the $n_{\rm e}^2$ dependence. Also, in the case of X-rays, the weaker dependence on the temperature makes T less relevant than in the SZ case.

In the outermost region 1, our model predicts slightly more X-rays than are actually observed both for the spherical and ellipsoid models. A decrease in the X-ray signal while maintaining the SZ effect can be obtained if the electron density is reduced by a factor $p < 1$ and the temperature is increased by a similar amount ($p^{-1} > 1$). The average SZ effect will remain the same while the X-ray average signal will decrease by a factor $p^{3/2}$. The small mismatch in region 1 could be an indication that the actual temperature in the outskirts of Virgo is higher than the one assumed in our model (1 keV for $r > 1$ Mpc). Another mechanism that can increase the X-ray to SZ ratio is gas clumping (Simionescu et al. 2011; Nagai & Lau 2011). If the gas

clusters in smaller clumps with enhanced local overdensities, this would result in an increase in the average X-ray emissivity while maintaining the average SZ signal. While clumpiness can not be ruled out in the outer parts of the cluster (and may offer a possible explanation for the observed signal), the fact that smooth models can simultaneously reproduce the central region in both SZ and X-ray data, suggests that the clumpiness mechanism, if present, must be small in the central regions. On the other hand Urban et al. (2011) argues that clumping may be responsible for the shallow profile observed by *XMM-Newton* in the outskirts of Virgo. Together with our results, this suggests that moderate clumpiness may be occurring in the outskirts of Virgo.

Adopting the gas masses derived from the ellipsoid model in Table 1, the total gas mass of the plasma is $(1.4–1.6) \times 10^{14}\,M_{\odot}$. If we assume the cosmic value for the baryon fraction, $f_{\rm b} = \Omega_{\rm b}/\Omega_{\rm m} = 0.1834$ (Planck Collaboration XIII 2016), the total mass of the cluster would be $(7.6–8.7)\times10^{14}\,M_{\odot}$, consistent with the upper values estimated from galaxy dynamics, like those based on the flow of galaxies falling into Virgo, from which Karachentsev et al. (2014) recently estimated a total mass for Virgo of $(8 \pm 2.3) \times 10^{14}\,M_{\odot}$.

7.3. Distance to the Virgo Cluster from SZ and X-ray data

In the above sections we have used the higher-end estimate of the distance to the Virgo cluster, motivated by the fact that we want to directly use recent estimates of the electron density in the central part of Virgo (as in G04). As noted in the introduction, the distance to the Virgo cluster is still a question of debate, with different values in the literature ranging from 16 to 21 Mpc. Hence, it is interesting to derive a new distance estimation based on the combined SZ and X-ray data (Silk & White 1978; Cavaliere et al. 1979; Birkinshaw et al. 1991; Herbig et al. 1995).

As described in Sect. 5.1, one can derive the electron density and temperature from X-rays, assuming a given distance, and compare the X-ray-derived pressure with the observed SZ effect. Since the deprojected electron density is proportional to the inverse of the square root of the distance, an agreement between the predicted and observed pressure should be obtained when the correct distance is assumed. In Fig. 14 above, we show an example of how the inferred gas pressure depends on the distance. In this case, the difference between the two pressures for the two distances is relatively small. This is a direct consequence of the weak dependency of the inferred electron density with the square root of the distance, $\sqrt{D}$.

A more sensitive distance discriminator can be derived from the gas mass. The estimation of the gas mass depends on the volume element, which is different for different distances. This is better understood if we define the volume element as the volume subtended by a fixed solid angle, like a cubic pixel. Hence, while the SZ and X-ray predicted signals are basically the same for different distances (once the volume elements and conversion rates are re-scaled according to the new distance), the estimated gas mass changes with distance as D^2. Figure 19 shows the dependence of the estimated mass of the gas on the distance to the cluster (note how the solid line passes through the value of the gas mass estimated in Sect. 7.2, assuming $D = 21$ Mpc). As expected, the gas mass grows as the square of the distance (from the combination of the volume element, $\propto D^3$, and the integral along the line of sight of the individual volume element, $\propto D^{-1}$). When compared with the gas mass estimated from the total mass and the cosmic baryon fraction we can obtain a direct estimate of the distance to the cluster. Adopting a mass range for Virgo

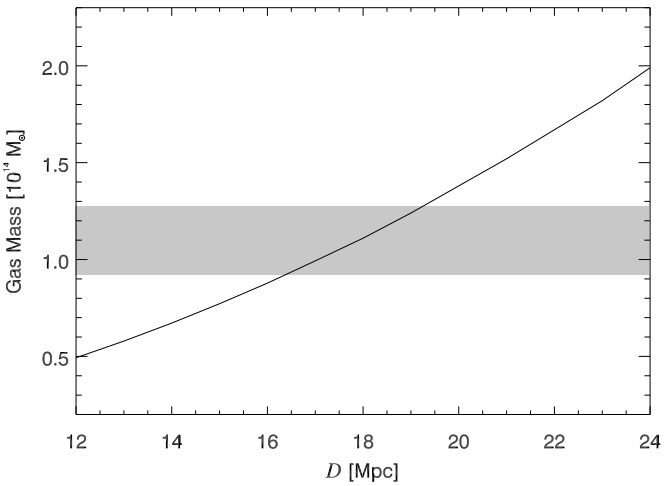

Fig. 19. Estimated gas mass (this work) as a function of distance (solid line). The shaded region corresponds to the gas mass derived assuming the total mass of the cluster can take values from $5 \times 10^{14}\,M_{\odot}$ to $7 \times 10^{14}\,M_{\odot}$ and that the fraction of mass corresponding to the gas equals the cosmic value, $f_{\rm b} = \Omega_{\rm b}/\Omega_{\rm m} = 0.1834$. The shaded region assumes also that different estimates of the total mass are independent of the distance.

from $5 \times 10^{14}\,M_{\odot}$ to $7 \times 10^{14}\,M_{\odot}$, which is consistent with the range of masses discussed in the introduction (de Vaucouleurs 1960; Hoffman et al. 1980; Böhringer et al. 1994; Karachentsev & Nasonova 2010; Karachentsev et al. 2014), and the cosmic value $f_{\rm b} = \Omega_{\rm b}/\Omega_{\rm m} = 0.1834$, we can infer the gas mass (shaded band in Fig. 19) and compare it with the solid curve in the same figure.

This simple test suggests that the distance to Virgo is around 18 Mpc, which fits nicely with the average estimate from different methods. Of course, this estimate relies on the assumption that the gas mass is known (or the total mass is known and the gas budget of the cluster up to the largest radii matches the cosmic value). If the distance (or redshift) is fixed, then the problem can be reversed to derive gas masses. This way of estimating distances to clusters could be of particular interest in future experiments (eROSITA, COrE+) where the estimation of the redshift of thousands of distant clusters may be a challenging task. Interestingly, this sensitivity to the redshift is a consequence of the relative insensitivity of the total SZ signal to redshift combined with the strong dependence of the total X-ray flux on redshift.

It is useful to put the inferred distance to Virgo of around 18 Mpc in the context of earlier estimates of the Hubble parameter based on the distance to Virgo. Pierce et al. (1994) found (based on Cepheids) a relatively small distance to Virgo of 14.9 Mpc and a corresponding $H_0 \approx 87\,{\rm km\,s^{-1}\,Mpc^{-1}}$. On the opposite extreme, the largest distance estimates to Virgo, $D \approx 21$ Mpc, come from 21-cm observations (Sandage & Tammann 1976; Federspiel et al. 1998), which also give a low estimate for $H_0 \approx 55\,{\rm km\,s^{-1}\,Mpc^{-1}}$. Rescaling the relatively small or large distances found by these authors to 18 Mpc would change the derived Hubble constant to $H_0 \approx 72\,{\rm km\,s^{-1}\,Mpc^{-1}}$ (for Pierce et al. 1994) or $H_0 \approx 64\,{\rm km\,s^{-1}\,Mpc^{-1}}$ (for Sandage & Tammann 1976; Federspiel et al. 1998). These values are in better agreement with the value derived from the power spectrum of the CMB by *Planck* (using TT, TE and EE constraints) of $H_0 = (67.6 \pm 0.6)\,{\rm km\,s^{-1}\,Mpc^{-1}}$. It is also important to highlight that the earlier estimates of H_0 based on SZ+X-ray measurement

found a value of $H_0 = (66 \pm 11)\,\mathrm{km\,s^{-1}\,Mpc^{-1}}$ (Jones et al. 2005), also in good agreement with the latest estimate from *Planck*.

8. Conclusions

Planck's full sky coverage, sensitivity, and wide frequency range offer the best opportunity to study the biggest single SZ source in the sky, the Virgo cluster. The combination of SZ with X-ray observations is a powerful way of constraining the gas properties in galaxy clusters. The strong dependence of X-rays on the electron density is particularly useful to constrain the gas density. However, in order to constrain the gas properties several assumptions have to be made. One common assumption is that the gas distribution is smooth, that is, there is no significant clumpiness. When comparing the X-ray-derived profiles in rings from Ghizzardi et al. (2004) and Urban et al. (2011) with the *Planck* SZ circular profile, we observe that the X-ray-derived profiles predict reasonably well the right amount of SZ signal without invoking the need for clumpiness to explain possible deviations. Another common assumption is that the cluster has spherical symmetry. We find that models derived from sparse *XMM-Newton* data and a spherical deprojection are able to reproduce the ring-averaged signal relatively well, both in X-rays and in the SZ effect within the virial radius (however, we note that in the X-ray domain the coverage of the outer regions with *XMM-Newton* and *Chandra* is sparse, limiting the diagnostic power of the X-ray/SZ comparison).

However, when the irregular geometry of Virgo is taken into account, the spherical model predicts significantly less SZ signal than observed beyond the virial radius. A model that breaks the spherical symmetry and concentrates the gas closer to the cluster plane (where the temperature should be higher) produces a better fit, suggesting an ellipsoidal distribution for Virgo. A prolate-like distribution with the longest axis (or axis of symmetry) in the image plane, (i.e., perpendicular to the line of sight) would be consistent with our model.

We study the signal in radial bins and find an excess in our SZ map reaching out to twice the virial radius. The observed signal is consistent with expectations from models based on an extrapolation of the electron density beyond the virial radius, with a power law $n_\mathrm{e} \propto r^{-1.2}$. The observed signal is also consistent with the expectation derived from a constrained simulation of Virgo. We observe that in order to reproduce the observed signal between R_vir and 2 R_vir with this power law, the temperature needs to be in the range of 1 keV beyond 1 Mpc from the cluster centre. The properties of this rarefied medium coincide with those expected for the hottest phase of the WHIM. Finally, using the estimated total gas mass inferred from the combination of SZ and X-ray data and under the assumption that the total baryon fraction of Virgo is representative of the cosmic value, we infer a distance to Virgo of approximately 18 Mpc.

Acknowledgements. The Planck Collaboration acknowledges the support of: ESA; CNES, and CNRS/INSU-IN2P3-INP (France); ASI, CNR, and INAF (Italy); NASA and DoE (USA); STFC and UKSA (UK); CSIC, MINECO, JA and RES (Spain); Tekes, AoF, and CSC (Finland); DLR and MPG (Germany); CSA (Canada); DTU Space (Denmark); SER/SSO (Switzerland); RCN (Norway); SFI (Ireland); FCT/MCTES (Portugal); ERC and PRACE (EU). A description of the Planck Collaboration and a list of its members, indicating which technical or scientific activities they have been involved in, can be found at http://www.cosmos.esa.int/web/planck/planck-collaboration. Some of the results presented in this work are based on observations obtained with *XMM-Newton* an ESA science mission with instruments and contributions directly funded by ESA Member States and NASA[5].

References

Anders, E., & Grevesse, N. 1989, Geochim. Cosmochim. Acta, 53, 197
Arnaud, K. A. 1996, in Astronomical Data Analysis Software and Systems V, eds. G. H. Jacoby, & J. Barnes, ASP Conf. Ser., 101, 17
Arnaud, M., Pratt, G. W., Piffaretti, R., et al. 2010, A&A, 517, A92
Birkinshaw, M., Hughes, J. P., & Arnaud, K. A. 1991, ApJ, 379, 466
Böhringer, H., Briel, U. G., Schwarz, R. A., et al. 1994, Nature, 368, 828
Burns, J. O., Skillman, S. W., & O'Shea, B. W. 2010, ApJ, 721, 1105
Cavaliere, A., Danese, L., & de Zotti, G. 1979, A&A, 75, 322
Churazov, E., Brüggen, M., Kaiser, C. R., Böhringer, H., & Forman, W. 2001, ApJ, 554, 261
Churazov, E., Forman, W., Jones, C., & Böhringer, H. 2003, ApJ, 590, 225
Cooray, A. R. 2000, MNRAS, 313, 783
Davé, R., Cen, R., Ostriker, J. P., et al. 2001, ApJ, 552, 473
Delabrouille, J., Cardoso, J., Le Jeune, M., et al. 2009, A&A, 493, 835
Despali, G., Giocoli, C., & Tormen, G. 2014, MNRAS, 443, 3208
de Vaucouleurs, G. 1960, ApJ, 131, 585
Diego, J. M., & Ascasibar, Y. 2008, MNRAS, 389, 1805
Dolag, K., Hansen, F. K., Roncarelli, M., & Moscardini, L. 2005, MNRAS, 363, 29
Federspiel, M., Tammann, G. A., & Sandage, A. 1998, ApJ, 495, 115
Fernández-Cobos, R., Vielva, P., Barreiro, R. B., & Martínez-González, E. 2012, MNRAS, 420, 2162
Forman, W., Jones, C., Churazov, E., et al. 2007, ApJ, 665, 1057
Freedman, W. L., Madore, B. F., Mould, J. R., et al. 1994, Nature, 371, 757
Fujimoto, R., Takei, Y., Tamura, T., et al. 2004, PASJ, 56, L29
Fukugita, M., Okamura, S., & Yasuda, N. 1993, ApJ, 412, L13
Ghizzardi, S., Molendi, S., Pizzolato, F., & De Grandi, S. 2004, ApJ, 609, 638
Górski, K. M., Hivon, E., Banday, A. J., et al. 2005, ApJ, 622, 759
Graham, J. A., Ferrarese, L., Freedman, W. L., et al. 1999, ApJ, 516, 626
Herbig, T., Lawrence, C. R., Readhead, A. C. S., & Gulkis, S. 1995, ApJ, 449, L5
Hirschmann, M., Dolag, K., Saro, A., et al. 2014, MNRAS, 442, 2304
Hoffman, G. L., Olson, D. W., & Salpeter, E. E. 1980, ApJ, 242, 861
Hurier, G., Macías-Pérez, J. F., & Hildebrandt, S. 2013, A&A, 558, A118
Jerjen, H., Binggeli, B., & Barazza, F. D. 2004, AJ, 127, 771
Jones, M. E., Edge, A. C., Grainge, K., et al. 2005, MNRAS, 357, 518
Kalberla, P. M. W., Burton, B. W., Hartmann, D., et al. 2005, A&A, 440, 775
Karachentsev, I. D., & Nasonova, O. G. 2010, MNRAS, 405, 1075
Karachentsev, I. D., Tully, R. B., Wu, P.-F., Shaya, E. J., & Dolphin, A. E. 2014, ApJ, 782, 4
Kenney, J. D. P., van Gorkom, J. H., & Vollmer, B. 2004, AJ, 127, 3361
Leach, S. M., Cardoso, J., Baccigalupi, C., et al. 2008, A&A, 491, 597
Lodders, K. 2003, ApJ, 591, 1220
Mathis, H., Lemson, G., Springel, V., et al. 2002, MNRAS, 333, 739
Mei, S., Blakeslee, J. P., Côté, P., et al. 2007, ApJ, 655, 144
Nagai, D., & Lau, E. T. 2011, ApJ, 731, L10
Pierce, M. J., Welch, D. L., McClure, R. D., et al. 1994, Nature, 371, 385
Planck Collaboration VIII. 2011, A&A, 536, A8
Planck Collaboration IX. 2011, A&A, 536, A9
Planck Collaboration X. 2011, A&A, 536, A10
Planck Collaboration Int. V. 2013, A&A, 550, A131
Planck Collaboration Int. X. 2013, A&A, 554, A140
Planck Collaboration XI. 2014, A&A, 571, A11
Planck Collaboration I. 2016, A&A, 594, A1
Planck Collaboration II. 2016, A&A, 594, A2
Planck Collaboration III. 2016, A&A, 594, A3
Planck Collaboration IV. 2016, A&A, 594, A4
Planck Collaboration V. 2016, A&A, 594, A5
Planck Collaboration VI. 2016, A&A, 594, A6
Planck Collaboration VII. 2016, A&A, 594, A7
Planck Collaboration VIII. 2016, A&A, 594, A8
Planck Collaboration XIII. 2016, A&A, 594, A13
Planck Collaboration XXII. 2016, A&A, 594, A22
Remazeilles, M., Delabrouille, J., & Cardoso, J.-F. 2011, MNRAS, 410, 2481
Roncarelli, M., Ettori, S., Dolag, K., et al. 2006, MNRAS, 373, 1339
Sandage, A., & Tammann, G. A. 1976, ApJ, 210, 7
Sereno, M., De Filippis, E., Longo, G., & Bautz, M. W. 2006, ApJ, 645, 170
Silk, J., & White, S. D. M. 1978, ApJ, 226, L103
Simionescu, A., Allen, S. W., Mantz, A., et al. 2011, Science, 331, 1576

[5] See list ObsID in Appendix B.

Simionescu, A., Werner, N., Urban, O., et al. 2015, ApJ, 811, L25
Smith, R. K., Brickhouse, N. S., Liedahl, D. A., & Raymond, J. C. 2001, ApJ, 556, L91
Snowden, S. L., Egger, R., Freyberg, M. J., et al. 1997, ApJ, 485, 125
Tammann, G. A., Sandage, A., & Reindl, B. 2000, Nucl. Phys. B Proc. Suppl., 80, C1311
Taylor, J. E., Moodley, K., & Diego, J. M. 2003, MNRAS, 345, 1127
Urban, O., Werner, N., Simionescu, A., Allen, S. W., & Böhringer, H. 2011, MNRAS, 414, 2101
Vikhlinin, A., Kravtsov, A., Forman, W., et al. 2006, ApJ, 640, 691
Werner, N., Simionescu, A., Million, E. T., et al. 2010, MNRAS, 407, 2063
Werner, N., ZuHone, J. A., Zhuravleva, I., et al. 2016, MNRAS, 455, 846
Yoon, J. H., Putman, M. E., Thom, C., Chen, H.-W., & Bryan, G. L. 2012, ApJ, 754, 84

[1] APC, AstroParticule et Cosmologie, Université Paris Diderot, CNRS/IN2P3, CEA/lrfu, Observatoire de Paris, Sorbonne Paris Cité, 10 rue Alice Domon et Léonie Duquet, 75205 Paris Cedex 13, France
[2] African Institute for Mathematical Sciences, 6-8 Melrose Road, Muizenberg 7945, Cape Town, South Africa
[3] Agenzia Spaziale Italiana Science Data Center, via del Politecnico snc, 00133 Roma, Italy
[4] Aix Marseille Université, CNRS, LAM (Laboratoire d'Astrophysique de Marseille), UMR 7326, 13388 Marseille, France
[5] Astrophysics Group, Cavendish Laboratory, University of Cambridge, J J Thomson Avenue, Cambridge CB3 0HE, UK
[6] Astrophysics & Cosmology Research Unit, School of Mathematics, Statistics & Computer Science, University of KwaZulu-Natal, Westville Campus, Private Bag X54001, 4000 Durban, South Africa
[7] Atacama Large Millimeter/submillimeter Array, ALMA Santiago Central Offices, Alonso de Cordova 3107, Vitacura, Casilla 763 0355, Santiago, Chile
[8] CGEE, SCS Qd 9, Lote C, Torre C, 4° andar, Ed. Parque Cidade Corporate, CEP 70308-200, Brasília, DF, Brazil
[9] CITA, University of Toronto, 60 St. George St., Toronto, ON M5S 3H8, Canada
[10] CNRS, IRAP, 9 Av. colonel Roche, BP 44346, 31028 Toulouse Cedex 4, France
[11] California Institute of Technology, Pasadena, California, CA 91125, USA
[12] Centro de Estudios de Física del Cosmos de Aragón (CEFCA), Plaza San Juan, 1, planta 2, 44001 Teruel, Spain
[13] Computational Cosmology Center, Lawrence Berkeley National Laboratory, Berkeley, California, USA
[14] DSM/Irfu/SPP, CEA-Saclay, 91191 Gif-sur-Yvette Cedex, France
[15] DTU Space, National Space Institute, Technical University of Denmark, Elektrovej 327, 2800 Kgs. Lyngby, Denmark
[16] Département de Physique Théorique, Université de Genève, 24, Quai E. Ansermet, 1211 Genève 4, Switzerland
[17] Departamento de Astrofísica, Universidad de La Laguna (ULL), 38206 La Laguna, Tenerife, Spain
[18] Departamento de Física, Universidad de Oviedo, Avda. Calvo Sotelo s/n, 33007 Oviedo, Spain
[19] Department of Astrophysics/IMAPP, Radboud University Nijmegen, PO Box 9010, 6500 GL Nijmegen, The Netherlands
[20] Department of Physics & Astronomy, University of British Columbia, 6224 Agricultural Road, Vancouver, British Columbia, Canada
[21] Department of Physics and Astronomy, Dana and David Dornsife College of Letter, Arts and Sciences, University of Southern California, Los Angeles, CA 90089, USA
[22] Department of Physics and Astronomy, University College London, London WC1E 6BT, UK
[23] Department of Physics, Florida State University, Keen Physics Building, 77 Chieftan Way, Tallahassee, Florida, USA
[24] Department of Physics, Gustaf Hällströmin katu 2a, University of Helsinki, 00014 Helsinki, Finland
[25] Department of Physics, Princeton University, Princeton, New Jersey, NJ 08544, USA
[26] Department of Physics, University of California, Santa Barbara, California, CA 93106, USA
[27] Department of Physics, University of Illinois at Urbana-Champaign, 1110 West Green Street, Urbana, Illinois, USA
[28] Dipartimento di Fisica e Astronomia G. Galilei, Università degli Studi di Padova, via Marzolo 8, 35131 Padova, Italy
[29] Dipartimento di Fisica e Scienze della Terra, Università di Ferrara, via Saragat 1, 44122 Ferrara, Italy
[30] Dipartimento di Fisica, Università La Sapienza, P.le A. Moro 2, 00185 Roma, Italy
[31] Dipartimento di Fisica, Università degli Studi di Milano, via Celoria 16, 20133 Milano, Italy
[32] Dipartimento di Fisica, Università degli Studi di Trieste, via A. Valerio 2, 34127 Trieste, Italy
[33] Dipartimento di Fisica, Università di Roma Tor Vergata, via della Ricerca Scientifica, 1, 00133 Roma, Italy
[34] Dipartimento di Matematica, Università di Roma Tor Vergata, via della Ricerca Scientifica, 1, 00133 Roma, Italy
[35] Discovery Center, Niels Bohr Institute, Blegdamsvej 17, Copenhagen, Denmark
[36] Discovery Center, Niels Bohr Institute, Copenhagen University, Blegdamsvej 17, 2100 Copenhagen, Denmark
[37] European Southern Observatory, ESO Vitacura, Alonso de Cordova 3107, Vitacura, Casilla 19001, Santiago, Chile
[38] European Space Agency, ESAC, Planck Science Office, Camino bajo del Castillo, s/n, Urbanización Villafranca del Castillo, Villanueva de la Cañada, Madrid, Spain
[39] European Space Agency, ESTEC, Keplerlaan 1, 2201 AZ Noordwijk, The Netherlands
[40] Facoltà di Ingegneria, Università degli Studi e-Campus, via Isimbardi 10, 22060 Novedrate (CO), Italy
[41] Gran Sasso Science Institute, INFN, viale F. Crispi 7, 67100 L'Aquila, Italy
[42] HGSFP and University of Heidelberg, Theoretical Physics Department, Philosophenweg 16, 69120 Heidelberg, Germany
[43] Helsinki Institute of Physics, Gustaf Hällströmin katu 2, University of Helsinki, 00014 Helsinki, Finland
[44] INAF–Osservatorio Astrofisico di Catania, via S. Sofia 78, Catania, Italy
[45] INAF–Osservatorio Astronomico di Padova, Vicolo dell'Osservatorio 5, 35122 Padova, Italy
[46] INAF–Osservatorio Astronomico di Roma, via di Frascati 33, 00040 Monte Porzio Catone, Italy
[47] INAF–Osservatorio Astronomico di Trieste, via G.B. Tiepolo 11, 40127 Trieste, Italy
[48] INAF/IASF Bologna, via Gobetti 101, 40129 Bologna, Italy
[49] INAF/IASF Milano, via E. Bassini 15, 20133 Milano, Italy
[50] INFN, Sezione di Bologna, via Irnerio 46, 40126 Bologna, Italy
[51] INFN, Sezione di Roma 1, Università di Roma Sapienza, Piazzale Aldo Moro 2, 00185 Roma, Italy
[52] INFN, Sezione di Roma 2, Università di Roma Tor Vergata, via della Ricerca Scientifica, 1, 00185 Roma, Italy
[53] INFN/National Institute for Nuclear Physics, via Valerio 2, 34127 Trieste, Italy
[54] IPAG: Institut de Planétologie et d'Astrophysique de Grenoble, Université Grenoble Alpes; CNRS, IPAG, 38000 Grenoble, France
[55] IUCAA, Post Bag 4, Ganeshkhind, Pune University Campus, 411 007 Pune, India
[56] Imperial College London, Astrophysics group, Blackett Laboratory, Prince Consort Road, London, SW7 2AZ, UK
[57] Infrared Processing and Analysis Center, California Institute of Technology, Pasadena, CA 91125, USA
[58] Institut Universitaire de France, 103 Bd Saint-Michel, 75005 Paris, France
[59] Institut d'Astrophysique Spatiale, CNRS (UMR 8617) Université Paris-Sud 11, Bâtiment 121, 91405 Orsay, France
[60] Institut d'Astrophysique de Paris, CNRS (UMR 7095), 98bis Boulevard Arago, 75014 Paris, France
[61] Institute of Astronomy, University of Cambridge, Madingley Road, Cambridge CB3 0HA, UK

[62] Institute of Theoretical Astrophysics, University of Oslo, Blindern, 0371 Oslo, Norway
[63] Instituto de Astrofísica de Canarias, C/Vía Láctea s/n, La Laguna, 38205 Tenerife, Spain
[64] Instituto de Física de Cantabria (CSIC-Universidad de Cantabria), Avda. de los Castros s/n, 39005 Santander, Spain
[65] Istituto Nazionale di Fisica Nucleare, Sezione di Padova, via Marzolo 8, 35131 Padova, Italy
[66] Jet Propulsion Laboratory, California Institute of Technology, 4800 Oak Grove Drive, Pasadena, California, USA
[67] Jodrell Bank Centre for Astrophysics, Alan Turing Building, School of Physics and Astronomy, The University of Manchester, Oxford Road, Manchester, M13 9PL, UK
[68] Kavli Institute for Cosmological Physics, University of Chicago, Chicago, IL 60637, USA
[69] Kavli Institute for Cosmology Cambridge, Madingley Road, Cambridge, CB3 0HA, UK
[70] Kazan Federal University, 18 Kremlyovskaya St., 420008 Kazan, Russia
[71] LAL, Université Paris-Sud, CNRS/IN2P3, Orsay, France
[72] LERMA, CNRS, Observatoire de Paris, 61 Avenue de l'Observatoire, Paris, France
[73] Laboratoire AIM, IRFU/Service d'Astrophysique – CEA/DSM – CNRS – Université Paris Diderot, Bât. 709, CEA-Saclay, 91191 Gif-sur-Yvette Cedex, France
[74] Laboratoire Traitement et Communication de l'Information, CNRS (UMR 5141) and Télécom ParisTech, 46 rue Barrault, 75634 Paris Cedex 13, France
[75] Laboratoire de Physique Subatomique et Cosmologie, Université Grenoble-Alpes, CNRS/IN2P3, 53 rue des Martyrs, 38026 Grenoble Cedex, France
[76] Laboratoire de Physique Théorique, Université Paris-Sud 11 & CNRS, Bâtiment 210, 91405 Orsay, France
[77] Lawrence Berkeley National Laboratory, Berkeley, California, USA
[78] Lebedev Physical Institute of the Russian Academy of Sciences, Astro Space Centre, 84/32 Profsoyuznaya st., GSP-7, 117997 Moscow, Russia
[79] Max-Planck-Institut für Astrophysik, Karl-Schwarzschild-Str. 1, 85741 Garching, Germany
[80] National University of Ireland, Department of Experimental Physics, Maynooth, Co. Kildare, Ireland
[81] Nicolaus Copernicus Astronomical Center, Bartycka 18, 00-716 Warsaw, Poland
[82] Niels Bohr Institute, Blegdamsvej 17, Copenhagen, Denmark
[83] Niels Bohr Institute, Copenhagen University, Blegdamsvej 17, Copenhagen, Denmark
[84] Optical Science Laboratory, University College London, Gower Street, London, UK
[85] SISSA, Astrophysics Sector, via Bonomea 265, 34136 Trieste, Italy
[86] School of Physics and Astronomy, Cardiff University, Queens Buildings, The Parade, Cardiff, CF24 3AA, UK
[87] Sorbonne Université-UPMC, UMR 7095, Institut d'Astrophysique de Paris, 98bis Boulevard Arago, 75014 Paris, France
[88] Space Research Institute (IKI), Russian Academy of Sciences, Profsoyuznaya Str, 84/32, 117997 Moscow, Russia
[89] Space Sciences Laboratory, University of California, Berkeley, California, CA 94720, USA
[90] Special Astrophysical Observatory, Russian Academy of Sciences, Nizhnij Arkhyz, Zelenchukskiy region, 369167 Karachai-Cherkessian Republic, Russia
[91] Sub-Department of Astrophysics, University of Oxford, Keble Road, Oxford OX1 3RH, UK
[92] The Oskar Klein Centre for Cosmoparticle Physics, Department of Physics, Stockholm University, AlbaNova, 106 91 Stockholm, Sweden
[93] UPMC Univ. Paris 06, UMR7095, 98bis Boulevard Arago, 75014 Paris, France
[94] Universität Heidelberg, Institut für Theoretische Astrophysik, Philosophenweg 12, 69120 Heidelberg, Germany
[95] Université de Toulouse, UPS-OMP, IRAP, 31028 Toulouse Cedex 4, France
[96] University Observatory, Ludwig Maximilian University of Munich, Scheinerstrasse 1, 81679 Munich, Germany
[97] University of Granada, Departamento de Física Teórica y del Cosmos, Facultad de Ciencias, 18071 Granada, Spain
[98] University of Granada, Instituto Carlos I de Física Teórica y Computacional, 18071 Granada, Spain
[99] Warsaw University Observatory, Aleje Ujazdowskie 4, 00-478 Warszawa, Poland

Appendix A: Stripe removal

One of the known artefacts of *Planck* data (and present in other experiments) are residuals from baseline removal, or "stripes". These stripes can produce fluctuations of several microkelvin (at 150 GHz) between neighboring scan trajectories. A discussion of the impact of stripes in the all-sky SZ map can be found also in Planck Collaboration XXII (2016). On small scales, these fluctuations can compete with and even dominate the weak SZ signals. Stripe residuals are small near the ecliptic poles where multiple scans overlap at different angles and they become greater near the ecliptic plane where the data are more noisy and the scan directions are nearly parallel to each other, making it harder to remove residual stripe signals. Since Virgo is located close to the ecliptic plane, stripes contaminate the SZ signal on small scales. These stripes are more evident in individual surveys, and hence individual survey maps can be used to isolate the stripe signal.

We produce SZ effect maps similar to the one described in the present paper, but based on individual surveys. The individual surveys are later combined in a destriping algorithm that removes stripe features. In the individual surveys, the stripe residuals tend to form elongated compact regions in Fourier space. These regions can be identified for each survey and depend on the scanning pattern of each survey. For a given survey, the "bad" modes in Fourier space can be substituted by the corresponding good modes in a different survey that does not show this feature in the same region of Fourier space. Alternatively, the compact region containing the bad modes can be identifed in Fourier space and this region can be masked out.

When transforming the Fourier modes back into real space we recover a destriped version of that survey. The difference between the two maps (original and destriped version) is shown in Fig. A.1. When smoothed with a 1°.5 FWHM Gaussian, the stripes contribute only a small fraction of a microkelvin and the biggest fluctuations do not affect the central region of Virgo. The effect of stripes is generally small on large scales and they tend to compensate each other when taking an average (as when computing profiles or smoothing the data). For instance, at 10′ resolution the stripes fluctuate, with amplitudes of about 4 μK at 143 GHz. When the same SZ map is smoothed with a 1°.5 FWHM Gaussian, the amplitude of the stripes falls below 1 μK.

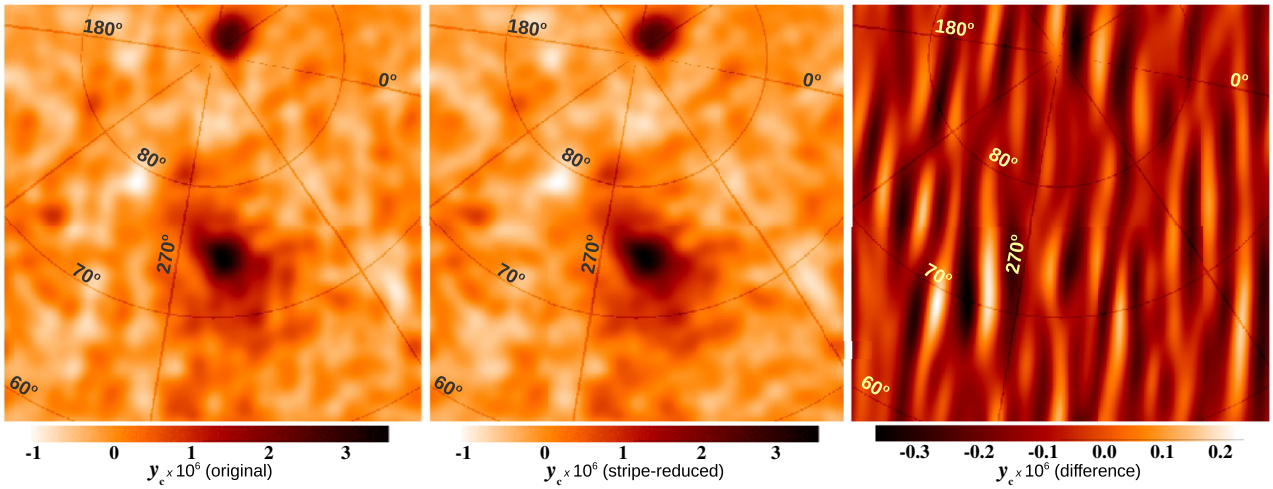

Fig. A.1. Estimation of the residual stripes in the SZ map in the Virgo region. All maps have been degraded to a resolution of 1°.5. *Left*: original data. *Middle*: stripe-reduced data. *Right*: difference between the original and the stripe-reduced maps. The colour bar in the right panel shows the difference in units of 10^7 times the Compton parameter; the colour scale in the other panels is the same as in Fig. 5.

Appendix B: *XMM-Newton* ObsIDs

This section lists the ObsIDs used in this work.

Table B.1. ObsIDs from the *XMM-Newton* public archive used for the X-ray analysis in Sect. 5.2.

0114120101	0200920101	0551870101	0551870301	0551870401	0551870501	0551870601	0551870701
0551871201	0551871301	0603260201	0603260401	0603260501	0603260601	0021540201	0106060201
0106060301	0106060401	0106060501	0106060601	0106060701	0106060801	0106060901	0106061101
0106061201	0106061401	0106860201	0108260201	0108860101	0110930301	0110930701	0112550501
0112550701	0112550801	0112551001	0112552101	0112610101	0112840101	0141570101	0145800101
0147610101	0200130101	0200650101	0202730301	0205010201	0208020101	0210270101	0210270201
0306060101	0306630101	0306630201	0404120101	0414980101	0502050101	0502050201	0502160101
0504100601	0504240101	0510011501	0550540101	0550540201	0556210601	0651790101	0651790201
0651790301	0673310101	0675140101					